# STUDY OF NEUTRON EMISSION IN ENERGETIC NUCLEAR COLLISIONS

*By*

**Manishsinh Ranajitsinh Gohil**

Enrolment No : PHYS04200904003

*Variable Energy Cyclotron Centre, Kolkata*

*A thesis submitted to the*

*Board of Studies in Physical Sciences*

*In partial fulfillment of requirements*

*for the Degree of*

**DOCTOR OF PHILOSOPHY**

*of*

**HOMI BHABHA NATIONAL INSTITUTE**


July, 2014

# Homi Bhabha National Institute

## Recommendations of the Viva Voce Committee

As members of the Viva Voce Committee, we certify that we have read the dissertation prepared by **Manish R Gohil** entitled **"Study of neutron emission in energetic nuclear collisions "** and recommend that it may be accepted as fulfilling the thesis requirement for the award of Degree of Doctor of Philosophy.

..... Alok Chakrabarti .....**Date:** 21.7.2014

**Chairman**- Dr. A. Chakrabarti

..... C. Bhattacharya .....**Date:** 21.7.2014

**Guide/Convener-** Dr. C.Bhattacharya

..... .....**Date:** 21/7/2014

**Member 1-** Dr. S.R.Banerjee

..... Satyajit Saha .....**Date:** 21/7/2014

**Member 2-** Dr. S. Saha

.....**Date:**

**Member 3-** Shri A. Roy 21/7/14

.....**Date:**

**Member 4-** Prof. D. Gupta 21/7/14

Final approval and acceptance of this thesis is contingent upon the candidate's submission of the final copies of the thesis to HBNI.

I hereby certify that I have read this thesis prepared under my direction and recommend that it may be accepted as fulfilling the thesis requirement.

**Date:** 21.7.2014

**Place:** Kolkata

C. Bhattacharya

Guide

# STATEMENT BY AUTHOR

This dissertation has been submitted in partial fulfillment of requirements for an advanced degree at Homi Bhabha National Institute (HBNI) and is deposited in the Library to be made available to borrowers under rules of the HBNI.

Brief quotations from this dissertation are allowable without special permission, provided that accurate acknowledgement of source is made. Requests for permission for extended quotation from or reproduction of this manuscript in whole or in part may be granted by the Competent Authority of HBNI when in his or her judgement the proposed use of the material is in the interests of scholarship. In all other instances, however, permission must be obtained from the author.

Manish R Gohil

# DECLARATION

I, hereby declare that the investigation presented in the thesis has been carried out by me. The work is original and has not been submitted earlier as a whole or in part for a degree/diploma at this or any other Institution/University.

Manish R Gohil

## List of Publications

# (A) List of Publications arising from the thesis

## (a) Journals

1. *"Measurement and simulation of neutron response function of organic liquid scintillator detector"*, **M. Gohil**, K. Banerjee, S. Bhattacharya, C. Bhattacharya, S. Kundu, T. K. Rana, G. Mukherjee, J. K. Meena, R. Pandey, H. Pai, T. K. Ghosh, A. Dey, S. Mukhopadhyay, D. Pandit, S. Pal, S. R. Banerjee, T. Bandopadhyay, **Nucl. Instr. and Meth. A 664, 304 (2012)**.

2. *"Angular momentum dependence of the nuclear level density parameter"*: **M. Gohil**, Pratap Roy, K. Banerjee, S. Bhattacharya, C. Bhattacharya, S. Kundu, T. K. Rana, T. K. Ghosh, G. Mukherjee, R. Pandey, J. K. Meena, H. Pai, V. Srivastava, A. Dey, Deepak Pandit, S. Mukhopadhyay, S. Pal, and S. R. Banerjee, **EPJ web of conferences 66,03073(2014)**.

3. *"Angular momentum dependence of the nuclear level density parameter for heavy mass nuclei"*: **M. Gohil**, Pratap Roy, K. Banerjee, S. Bhattacharya, C. Bhattacharya, S. Kundu, T. K. Rana, T. K. Ghosh, G. Mukherjee, R. Pandey, J. K. Meena, H. Pai, V. Srivastava, A. Dey, Deepak Pandit, S. Mukhopadhyay, S. Pal, and S. R. Banerjee, in preparation.

## (b) Conference Proceedings

1. *"Geant4 simulation of pulse-height response function of liquid scintillator based neutron detector"*: **M. Gohil**, K. Banerjee, C. Bhattacharya, S. Kundu, T. K.Rana, G. Mukherjee, J. K.Meena, R. Pandey, H. Pai, M. Biswas, A. Dey, T. Bandhopadhyay, and S. Bhattacharya, Proc. of DAE- BRNS symposium on Nucl. Phys. Vol. 55 (Part II), 720 (2010).

2. *"Low energy neutron response function of BC501A detector : comparison with GEANT-4 simulation"*: **M. Gohil**, K. Banerjee, C. Bhattacharya, S. Kundu, T. K. Rana, G. Mukherjee, R. Pandey, H. Pai, P. Roy, T. K. Ghosh, J. K. Meena and S. Bhattacharya, Proc. of DAE- BRNS symposium on Nucl. Phys. Vol. 56 , 1046 (2011).

3. *"Study of nuclear level density parameter using neutron"*: **M. Gohil**, K. Banerjee, C. Bhattacharya, S. Kundu, T. K. Rana, G. Mukherjee, J. K.Meena, R. Pandey, H. Pai1, M.Biswas, A. Dey, T. Bandhopadhyay, and S. Bhattacharya, Proc. of DAE- BRNS symposium on Nucl. Phys. Vol. 57, 494 (2012).

4. *"Angular Momentum Dependence of Nuclear Level Density Parameter"*: Pratap Roy, K. Banerjee, **M. Gohil**, S. Bhattacharya, C. Bhattacharya, S. Kundu, T. K. Rana, T. K. Ghosh, G. Mukherjee, R. Pandey, J. K. Meena, H. Pai, V. Srivastava, A. Dey, Deepak Pandit, S. Mukhopadhyay, S. Pal, and S. R. Banerjee, Book of Abstracts 03 - Nuclear Reactions, International Nuclear Physics Conference INPC2013: 2-7 June 2013, Firenze, Italy, NR 169.

# (B) Other Publications

## (a) Journals

1. *"Effect of collectivity on the nuclear level density"* : Pratap Roy, K. Banerjee, **M. Gohil**, C. Bhattacharya, S. Kundu, T. K. Rana, T. K. Ghosh, G. Mukherjee, R. Pandey, H. Pai, V. Srivastava, J. K. Meena, S. R. Banerjee, S. Mukhopadhyay, D. Pandit, S. Pal, and S. Bhattacharya, Phys. Rev. C 88, 031601(R) (2013).

2. *"Band structures and intruder $i_{13/2}$ state in $^{197}Tl$"*: H. Pai, G. Mukherjee, S. Bhattacharya, C. Bhattacharya, S. Bhattacharyya, T. Bhattacharjee, S. Chanda, S. Rajbanshi, A. Goswami, **M. R. Gohil**, S. Kundu, T. K. Ghosh, K. Banerjee, T. K. Rana, R. Pandey, G. K. Prajapati, S. R. Banerjee, S.

Mukhopadhyay, D. Pandit, S. Pal, J. K. Meena, P. Mukhopadhyay, and A. Choudhury, Phys. Rev. C 88, 064302 (2013).

3. *"Estimation of direct components of the decay of the Hoyle state"*: T. K. Rana, S. Bhattacharya, C. Bhattacharya, S. Kundu, K. Banerjee, T. K. Ghosh, G. Mukherjee, R. Pandey, P. Roy, V. Srivastava, **M. Gohil**, J. K. Meena, H. Pai, A. K. Saha, J. K. Sahoo, and R. M. Saha, Phys. Rev. C 88, 021601(R) (2013).

4. *"Angular-momentum-gated light-particle evaporation spectra from* $^{97}Tc$ *and* $^{62}Zn$ *systems"*, Pratap Roy, K. Banerjee, S. Bhattacharya, C. Bhattacharya, S. Kundu, T. K. Rana, T. K. Ghosh, G. Mukherjee, R. Pandey, J. K. Meena, **M. Gohil**, H. Pai, V. Srivastava, A. Dey, Deepak Pandit, S. Mukhopadhyay, S. Pal, and S. R. Banerjee, Phys Rev C 86, 044622 (2012).

5. *"High spin band structures in doubly odd* $^{194}Tl$*"*: H. Pai, G. Mukherjee, S. Bhattacharyya, **M. R. Gohil**, T. Bhattacharjee, C. Bhattacharya, R. Palit, S. Saha, J. Sethi, T. Trivedi, Shital Thakur, B. S. Naidu, S. K. Jadav, R. Donthi, A. Goswami, S. Chanda, Phys. Rev. C 85, , 064313 (2012).

6. *"Variation of nuclear level density with angular momentum"*: K. Banerjee, S. Bhattacharya, C. Bhattacharya, **M. Gohil**, S. Kundu, T. K. Rana, G. Mukherjee, R. Pandey, P. Roy, H. Pai, A. Dey, T. K. Ghosh, J. K. Meena, S. Mukhopadhyay, D. Pandit, S. Pal, and S. R. Banerjee, Phys Rev C 85, 064310 (2012).

7. *"Measurement of Giant Dipole Resonance width at low temperature: A new experimental perspective"*, S. Mukhopadhyay, Deepak Pandit , Surajit Pal, Srijit Bhattacharya, A. De, S. Bhattacharya, C. Bhattacharya, K. Banerjee, S. Kundu, T. K. Rana, G. Mukherjee, R. Pandey, **M. Gohil**, H. Pai, J. K. Meena and S. R. Banerjee, Phys Lett B 709, 9 (2012).

## (b) Conference Proceedings

1. *"Signature of collective enhancement in nuclear level density"* : Pratap Roy, K. Banerjee, **M. Gohil**, C.Bhattacharya, S. Kundu,T. K. Rana,T. K. Ghosh,G. Mukherjee,R. Pandey,H. Pai,V. Srivastava, J. K. Meena,S. R. Banerjee,S. Mukhopadhyay,D. Pandit,S. Pal, S. Bhattacharya, Proceedings of the International symposium on nuclear physics, BARC, Mumbai, India, Vol 58, Page 378 (2013).

2. *"Search for rotational state of Hoyle state in complete kinematic experiment* $^{12}C(\alpha, \alpha)3\alpha$ *"*: C. Bhattacharya, T. K. Rana, S. Bhattacharya, S. Kundu, K. Banerjee, T. K. Ghosh, G. Mukherjee, R. Pandey, **M. Gohil**, A. Dey, J. K. Meena, G. Prajapati, P. Roy, H. Pai, M. Biswas, Book of Abstracts 03 - Nuclear Reactions, International Nuclear Physics Conference INPC2013: 2-7 June 2013, Firenze, Italy , NR 019.

3. *"Further limit on* $3\alpha$ *decay of Hoyle state"*: T. K. Rana, S. Bhattacharya, C. Bhattacharya, S. Kundu, K. Banerjee, T. K. Ghosh, G. Mukherjee, R. Pandey, P. Roy, V. Srivastava, **M. Gohil**, J. K. Meena, H. Pai, A. K. Saha, J. K. Sahu, Book of Abstracts 03 - Nuclear Reactions, International Nuclear Physics Conference INPC2013: 2-7 June 2013, Firenze, Italy, NR 164.

4. *"Study of angular momentum gated light-particle evaporation spectra in* $^{4}He$ *+* $^{93}Nb$ *and* $^{4}He$ *+* $^{58}Ni$ *reactions"* : Pratap Roy, K. Banerjee, S. Kundu, T. K. Rana, T.K. Ghosh, C. Bhattacharya, G. Mukherjee, R. Pandey, J. K. Meena, **M. Gohil**, H. Pai, V. Srivastava, A. Dey, S. Mukhopadhyay, D. Pandit, S. Pal, S. R. Banerjee, and S. Bhattacharya, Proc. of DAE- BRNS symposium on Nucl. Phys. Vol. 57, 420 (2012).

5. *"Search of* $2_2^+$ *state of Hoyle state of* $^{12}C$ *"*: T. K. Rana, S. Bhattacharya, C. Bhattacharya, S. Kundu, K. Banerjee, T. K. Ghosh, G. Mukherjee, R. Pandey,**M. Gohil**, A. Dey, J. K. Meena, G. Prajapati, P. Roy, H. Pai, M.

Biswas, Proc. of DAE- BRNS symposium on Nucl. Phys. Vol. 57, 422 (2012).

6. *"Elastic scattering of alpha particles from $^{27}Al$ target"*: Aparajita Dey, S. Ganguly, V. Srivastava, T.K. Rana, S. Kundu, K. Banerjee, H. Pai, C. Bhattacharya, T.K. Ghosh, R. Pandey, G. Mukherjee, J.K. Meena, **M.R. Gohil**, and S. Bhattacharya, Proc. of DAE- BRNS symposium on Nucl. Phys. Vol. 57, 438 (2012).

7. *"($\alpha$,$^3He$) and ($\alpha$,$^3H$) transfer reaction studies at $E_\alpha$=60 MeV"* : R. Pandey, A. Dey, T. K. Rana, M. Biswas, T. K .Ghosh, C. Bhattacharya, S. Kundu, K. Banerjee, G. Mukherjee, P. Roy, J. K. Meena, V. Srivastava, H. Pai, **M. Gohil**, S. Bhattacharya, Proc. of DAE- BRNS symposium on Nucl. Phys. Vol. 57, 526 (2012).

8. *"Charged particle detector array: $45^0$-$175^0$"* : S. Kundu, C. Bhattacharya, T. K. Rana, K. Banerjee, S. Bhattacharya, J. K. Meena, R. Saha, G. Mukherjee, T. K. Ghosh, R. Pandey, P. Roy, **M. Gohil**, V. Srivastava, A. Dey, G. Pal, S. Roy, S. R. Bajirao, C. Nandi, Proc. of DAE- BRNS symposium on Nucl. Phys. Vol. 57, 864 (2012).

9. *"Development of a low pressure PPAC for detection of heavy charged particles"*: R. Pandey*, T. K. Ghosh, J. K. Meena, K. Banerjee, C. Bhattacharya, S. Bhattacharya, **M. Gohil**, G. Mukherjee, S. Kundu, T. K. Rana, P. Roy, H. Pai, V. Srivastava, Proc. of DAE- BRNS symposium on Nucl. Phys. Vol. 57, 930 (2012).

10. *"Coexistence of different band structures in odd-odd $^{194}Tl$"*: H. Pai, G. Mukherjee, S. Bhattacharyya, **M.R. Gohil**, C. Bhattacharya, R. Palit, A. Goswami, T. Bhattacharjee, S. Saha, J. Sethi, T. Trivedi, S. Thakur ,B.S. Naidu, S.K. Jadav, and R. Donthi , Proc. of DAE- BRNS symposium on Nucl. Phys. Vol. 56 , 198 (2011).

11. *"Gamma ray spectroscopy of $^{197}Tl$ using $\alpha$ beam"*: H. Pai, G. Mukherjee, A. Goswami, S. Bhattacharyya, S. Chanda, T. Bhattacharjee, C. Bhattacharya, S. Bhattacharya, K. Banerjee, S. R. Banerjee, A. Chowdhury, P. Chowdhury, T.K. Ghosh, **M. R. Gohil**, S. Kundu, J.K. Meena, P. Mukhopadhyay, S. Mukhopadhyay, S. Pal, R. Pandey, D. Pandit, G. Prajapati,S. Rajbangshi , and T.K. Rana , Proc. of DAE- BRNS symposium on Nucl. Phys. Vol. 56 , 286 (2011).

12. *"Structure and decay mechanism of Hoyle state"*: T. K. Rana, S. Bhattacharya, C. Bhattacharya, S. Kundu, K. Banerjee, G. Mukherjee, J. K. Meena, R. Pandey, **M. Gohil**, H. Pai, A. Dey, T. K. Ghosh, M. Biswas, G. Prajapati, Proc. of DAE- BRNS symposium on Nucl. Phys. Vol. 56 , 492 (2011).

13. *"Study of light-particle evaporation spectra (n, p, $\alpha$) in $^{4}He+$ $^{93}Nb$ reaction"*: Pratap Roy, K. Banerjee, S. Kundu, T. K. Rana, C. Bhattacharya, **M. Gohil**, G. Mukherjee, J. K. Meena, R. Pandey, H. Pai, A. Dey, T.K. Ghosh, S. Mukhopadhyay, D. Pandit, S. Pal, S. R. Banerjee, and S. Bhattacharya , Proc. of DAE- BRNS symposium on Nucl. Phys. Vol. 56 , 540 (2011).

14. *"Extraction of angular momentum gated nuclear level density parameter"* : K. Banerjee, C. Bhattacharya, **M. Gohil**, S. Kundu, T. K. Rana, G. Mukherjee, R. Pandey, H. Pai, Pratap Roy, T. K. Ghosh, J. K. Meena, S.Mukhopadhyay, D. Pandit, S. Pal, S. R. Banerjee, and S. Bhattacharya, Proc. of DAE- BRNS symposium on Nucl. Phys. Vol. 56 , 594 (2011).

15. *"Angular momentum gated neutron evaporation studies"*: K. Banerjee, S. Kundu, T. K. Rana, C. Bhattacharya, G. Mukherjee, **M.Gohil**, J. K. Meena, R. Pandey, H. Pai, A. Dey, M. Biswas, S. Mukhopadhyay, D. Pandit, S. Pal, S. R. Banerjee, T. Bandhopadhyay and S. Bhattacharya, Proc. of DAE- BRNS symposium on Nucl. Phys. Vol. 55 (Part II), 324 (2010).

Manish R Gohil

# ACKNOWLEDGEMENTS

First of all, I would like to thank my supervisor Dr. Chandana Bhattacharya for her help, valuable guidance and encouragement during my PhD work. I gratefully acknowledge Dr. Sailajananda Bhattacharya for his advise, supervision and valuable contribution to this work. I wish to express my gratitude to Dr. Kaushik Banerjee for his constant suggestions and help throughout the past five years.

I would like to give some special thanks to my year mates Arnab Banerjee, Somnath De, Sudipan De, Nihar Sahoo and Yunus as well as to my Seniors Pratap Roy, Tapan Rana, Dr. Samir Kundu, Dr. Gopal Mukherjee, R Panday, Dr. T K Ghosh, Dr. D Pandit ,V Srivastava, Jay Kiran Meena and at last to all my juniors.

Words of acknowledgment remain incomplete if I do not express my sincere and deep sense indebtedness to my family members.

# Contents

# SYNOPSIS

A systematic understanding of the properties of hot nuclei can be made by studying the light partciles (n, p,d,t,$\alpha$) evaporated from the hot nuclear system. The statistical model has been often used to predict the distribution of evaporated particles from the excited compound nucleus populated by the energetic collision and subsequently the fusion of the target and the projectile. In statistical model, the particle emission probabilities are linked with the corresponding available phase spaces, which in turn are crucially dpendent on the nuclear level density. So, nuclear level density plays a key role in statistical model analysis of evaporation spectra, and accurate determination of nuclear level density (NLD) and its dependence on excitation energy, atomic mass and angular momentum, is required to predict the cross-sections using statistical model. The dependence of level density on atomic mass and excitation are fairly well established. However, information available about the angular momentum dependence of level density is quite limited. In recent years, a few studies on the angular momentum dependance of NLD have been made in low and medium mass nuclei. In the present thesis work, detailed experimental study of the angular momentum dependence of nuclear level density for the heavy nuclei in the mass region (A $\sim$ 170-200) have been made by measuring the energy distribution of emitted neutrons in coincidence with $\gamma$ - ray mulciplicity. The compound systems $^{169}$Tm, $^{185}$Re and $^{201}$Tl have been populated at different excitations using the reactions $^{4}$He + $^{165}$Ho, $^{4}$He + $^{181}$Ta and $^{4}$He + $^{197}$Au respectively, at 28 - 40 MeV beam energies. The experiment were performed at VECC. Energy spectra of the evaporated neutrons have been measured in coincidence with the $\gamma$-rays of different multiplicities (folds) using liquid - scintillator (BC501A) detectors, by time of flight technique whereas the neutron gamma discrimination was achieved by both pulse shape discrimination (PSD) and time of flight. In the present experiment, populated angular momenta were recorded by measuring the $\gamma$- multiplicity using a 50 element $BaF_2$ based low energy $\gamma$-ray filter array. The fold-gated neutron energy spectra were measured to study the angular momentum dependency of NLD. The

number of $BaF_2$ detectors fired simultaneously in an event provides the fold, which is directly related to the compound nucleus angular momentum. Angular momentum distribution was then extracted from the measured $\gamma$-ray fold distribution using Monte Carlo calculation based on GEANT3 toolkit. The Theoretical neutron energy spectra for different $\gamma$-ray multiplicities were estimated by the statistical model code CASCADE using the extracted angular momentum distributions for different folds as the input. Then the level density parameter was extracted by comparing the experimental neutron energy spectrum with that calculated using statistical model code CASCADE by $\chi^2$ minimization technique. It has been observed that the level density parameter remained constant as angular momentum increases for all three systems at all excitation energies used in present work. This trend is differenet from those observed in lighter systems, where NLD was found to be sensitive with the change in angular momentum. This behaviour of NLD over the whole mass range is yet to be understood theoretically.

The present thesis is also devoted to the study of measurement and simulation of neutron response function of organic liquid scintillator detector. Organic liquid scintillator (BC501A) based detectors were developed in - house to measure the energy of neutrons using time of flight (TOF) techniques. Detectors of various dimensions were fabricated to study various characteristics of detectors like pulse height response, absolute efficiency, neutron-$\gamma$ discrimination, etc. Neutron and $\gamma$-ray pulse-height responses of the neutron detector were simulated using GEANT4 toolkit ( version 4.9.2 ).

Experimental $\gamma$-ray pulse height response obtained using standard photon source $^{137}Cs$ was compared with GEANT4 simulated result. GEANT4 simulation has also been compared with the corresponding simulation done using the standard photon response code PHRESP, which is known to be very good in the photon energy range $\leq$ 20 MeV. It was seen that GEANT4 simulation was in good agreement with the data as well as with the PHRESP simulation at energies around the Compton edge; however, both GEANT4 as well as PHRESP calculations differ slightly from the

experiment at lower pulse heights.

Mono-energetic neutron pulse height response functions have been simulated using GEANT4 and compared with experimentally measured data in the energy range 2 - 20 MeV. The experimental neutron response functions have been obtained from the present measurement as well as from the literature. The response functions of monoenergetic neutrons of energies below $\leq$6 MeV have been extracted from the corresponding neutron energy spectrum obtained from the $^{252}$Cf neutron source. The neutron energy spectrum has been measured using time-of-flight(TOF) method, where start was taken from $BaF_2$ detector array and stop from liquid scintillator detector. The neutron events have been separated from the $\gamma$-ray events using pulse shape discrimination (PSD) technique. The mono energetic neutron response has been extracted from the measured continuous neutron energy spectrum by selecting appropriate TOF-window in the TOF spectrum. The experimental neutron response function for neutrons of energies >6 MeV have been taken from the literature.

Measured neutron response function obtained at different neutron energies have been compared with the results obtained using GEANT4 and NRESP7 code. It was found that, for neutron energies <7 MeV, the measured response functions are well reproduced by both GEANT4 simulation as well as by NRESP7 code. It was also found that for neutron of enenegies >7MeV, though the response functions were well reproduced by NRESP7 code, GEANT4 simulation could not predict the response functions, in particular to lower pulse height. The reasons for discrepancies between the experimental and the GEANT4 simulated responses at lower pulse heights are due to the incompleteness of the physics processes NeutronHP model included in GEANT4 calculations. At higher neutron energies ( E>8 - 10 MeV )more reaction channels open up, giving rise to higher discrepancies. Higher order reaction channels like $^{12}$C(n , $\alpha$)$^{9}$Be$^{*}$ $\rightarrow$ 2$\alpha$ + n, $^{12}$C(n , n')$^{12}$C$^{*}$ $\rightarrow$ 3$\alpha$ become very important and should be properly taken into account.

Attempts have also been made in the present thesis to check the usefulness of other available models in comparison to NeutronHP models, which are designed

specifically for low energy neutrons upto 20 MeV. It was seen that NeutronHP models provide better agreement with the experimental data. The use of another cross-sectional data library, i.e., G4HadronDaSet has also been found to make no qualitative difference.

# List of Figures

# List of Tables

# Chapter 1

# INTRODUCTION

The study of nuclear reaction is very important for number of reasons. There are many nuclear reactions that play important role in human life. For example, human life on the earth would not be possible without the energy provided to human by the sun. This energy is released from the nuclear reactions that occur in the sun. When a collision occurs between moving projectile and target, either the projectile scatters elastically or the ejectile ( projectile / target / the reaction product) is excited and subsequently decays by emitting one or more nucleons, complex particles or gamma rays. A nuclear reaction is characterized by identifying projectile, target and products. There are some conservation rules that must be applied to any nuclear reaction equations.

1. Mass number $A$ and atomic number $Z$ must be equal in each side of nuclear reaction equation.

2. The total energy must be conserved. That means the total energy before the reaction must be equal to the total energy after the reaction.

3. The total momentum before the reaction must be equal to the total momentum after the reaction.

4. Angular momentum, parity and isospin are governed by respective quantum conservation rules.

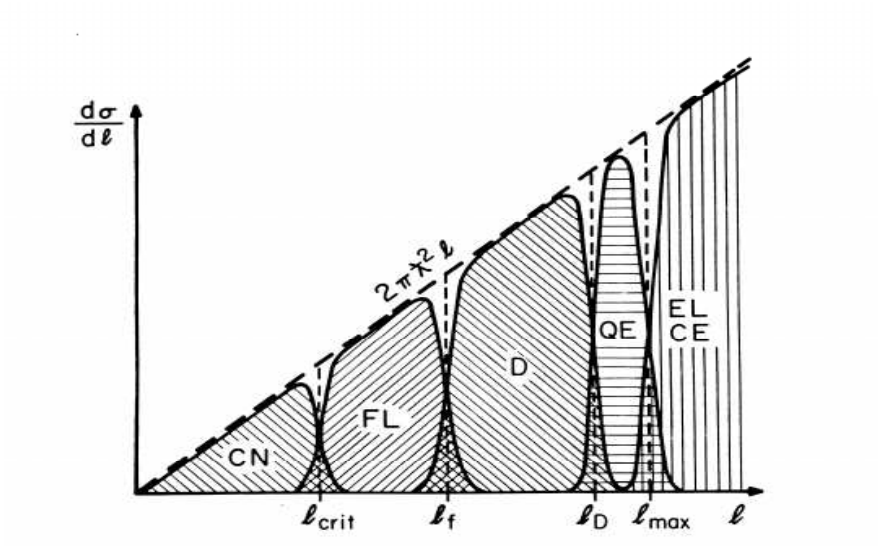


Figure 1.1: Schismatic diagram of the $l$ dependence of partial reaction cross sections.

There are so many types of nuclear reactions which occur during the interaction between the target and the projectile. Some examples include: elastic scattering, inelastic scattering, fusion, knockout, transfer reactions and so on. Based on the reaction mechanism, nuclear reactions are mainly classified in two categories: (1) Direct reactions and (2) compound nuclear reactions [1]. Range of the reaction channel can be described in terms of impact parameter and vis-a-vis angular momentum transfer associated with each of the reaction mechanisms. Angular momentum and impact parameter dependence of partial cross sections of compound nucleus ( CN ), fusion-like ( FL ), deep inelastic ( DE ), quasi elastic( QE ), Coulomb excitations ( CE ) and elastic processes are shown in Figs 1.1 and 1.2, respectively. The most peripheral collisions lead to elastic scattering. Grazing collisions lead to quasi-elastic scattering and other direct reactions. Solid contact collisions lead to deep inelastic collision, which is intermediate between direct and CN reaction. Most head-on collision lead to fusion and the formation of compound nucleus.

1. **Direct reactions**

In direct nuclear reactions, projectile interact mainly at the surface of the target nucleus and therefore such reactions are also called peripheral reaction processes. High energetic projectile interacts with only a few nucleons of the target nucleus instead of the target nucleus as a whole because of its small De Broglie wavelength. There are primarily two differences between direct and compound nuclear reactions:(1) Direct reactions take place very rapidly, in a time of order of $10^{-22}s$, while compound nuclear reactions take much longer time, possibly $\sim 10^{-16}s$ [1]. This additional time is required for the distribution and re-concentration of the projectile energy. (2) Angular distribution of the emitted particles in direct nuclear process tend to be forward peaked in contrast to the symmetric angular distribution likely in the case of compound nuclear processes. Depending on the energy of the projectile particle, the reaction process can proceed either through a direct reaction or a compound nuclear reaction.

2. **Compound nuclear reactions**

   Compound nuclear reactions are discussed in detail in next paragraphs.

## 1.1 Compound nuclear reactions

Compound nuclear reaction is low energy nuclear reaction and was first explained by N.Bohr in 1936. In many low energy nuclear reactions, the incident nucleus fuses with the target nucleus to form compound system in an excited state which subsequently decays by particle evaporation. At low energy, such type of reaction is characterized by sharp peaks ( resonance ) in the excitation function ( cross section as function of energy ). Such small width in energy indicates relatively long time $\tau$ associated with this process. This feature indicates that a quantum mechanical treatment is necessary in analysis of such process. At higher energy (typically above excitation energy $> 10$ MeV ), it is observed that resonances start to overlap, which means that the time scale is faster and reaction process is determined by average effect of many levels forming quasi-continuum; and so statistical treatment

can be used. Due to long time associated with compound nuclear reactions, Bohr proposed that energy of incident particle is shared equally with all nucleons of the combined system of projectile plus target. The average increase in energy of any single nucleon is not enough to free it from the nucleus. But due to random collisions among the nucleons, there is small but finite probability for a single nucleon to gain enough energy to escape. Subsequently, long after the capture of incident nucleus, particles are evaporated by statistical process leading to some final state of the residual nucleus. The reactions proceed through a definite intermediate state after the capture of the incident particle. Such intermediate state, which is fully equilibrated in all degrees of freedom, is called the compound nucleus. So, the reaction with projectile $a$ and target $X$

$$a + X \rightarrow Y + b \tag{1.1}$$

can be written as [1]

$$a + X \rightarrow C^* \rightarrow Y + b \tag{1.2}$$

where $C^*$, $Y$ and $b$ are compound nucleus, residual nucleus and emitted particle, respectively. According to this model, this type of reaction is two step process: (a) the formation of compound nucleus, and (b) subsequent decay of the compound nucleus [1]. The assumption of this model is that decay process of compound nucleus is independent of the formation process of compound nucleus. Decay probability depends only on the total energy and angular momentum of the compound nucleus. The compound nucleus model works best for medium and heavy nuclei, where the nuclear interior is large enough to absorb the incident energy of projectile. Another feature of compound nucleus reaction is the angular momentum distribution of the products. As the nucleons in a compound nucleus are assumed to be in full thermal equilibrium, it is expected that angular distribution of out-going particle is symmetric around $90^\circ$ in the center of mass frame. This expectation is consistent with experiment.

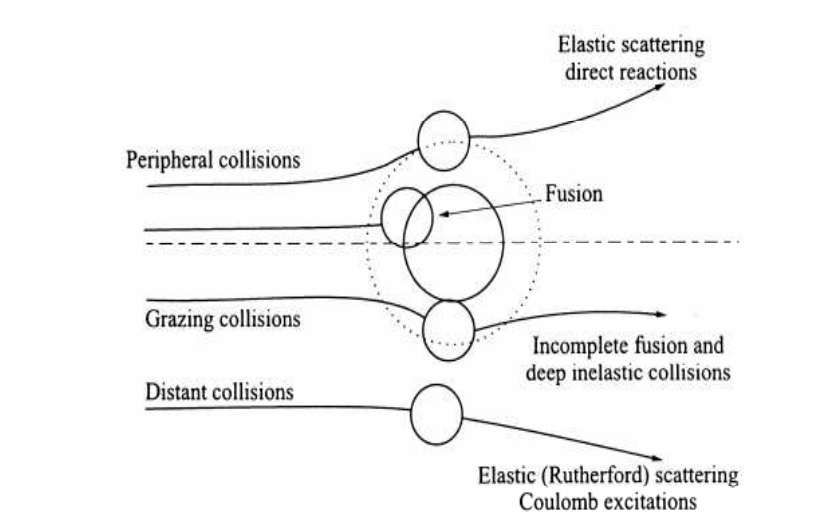


Figure 1.2: Classification of collision based upon impact parameter.

### 1.1.1 Compound reaction cross section

The cross section of the compound reaction can be written as [2, 3]

$$\sigma_{ab} = \sigma_a \frac{\tau_b}{\tau} \tag{1.3}$$

where $\sigma_a$ is the formation cross section of the compound nucleus $C^*$, $\tau$ is the total decay width of the compound nucleus $C^*$ and $\tau_b$ is the decay width of the reaction channel $b$. When the projectile $(a)$ enters the target nucleus $(X)$, it interacts with the nucleons of $X$ and shares its energy with all nucleons of $X$ to reach equilibrium and then form the excited compound nucleus $C^*$ . The excitation energy states are well separated for low excitations, so the cross section has resonance pattern. For higher excitations, the energy states are continuous, so the cross section varies slowly with energy [4, 5], which is called continuum region. The transition from resonance to continuum depends on the energy and mass number $A$. The excited compound nucleus decays by emitting a number of nucleons or complex fragments. The total cross section is [3]

$$\sigma_{tot} = \frac{4\pi}{k}\sum_{l=0}^{\infty}(2l+1)Imf_l(0) \tag{1.4}$$

which can be simplified as

$$\sigma_{tot} = \frac{4\pi}{k^2}\sum_{l=0}^{\infty}(2l+1)Sin^2\delta_l(E) \tag{1.5}$$

where

$$f_l = \frac{S_l - 1}{2ik} \tag{1.6}$$

with

$$S_l = \exp(2i\delta_l(k)) \tag{1.7}$$

when $\delta_l(E)$ satisfy the condition

$$\delta_l(E) \sim (n + \frac{1}{2})\pi \tag{1.8}$$

or

$$Sin^2\delta_l(E) \sim 1 \tag{1.9}$$

partial wave cross section reaches its maximum value and therefore resonance occur. If we expand near resonance energy $E = E_0$

$$Sin\delta_l(E) \approx Sin\delta_l(E_0) + \left[Cos\delta_l(E)\frac{d\delta_l}{dE}\right]_{E_0}(E - E_0) \approx 1 \tag{1.10}$$

here we have

$$Cos\delta_l(E) \approx Cos\delta_l(E_0) - \left[Sin\delta_l(E)\frac{d\delta_l}{dE}\right]_{E_0}(E - E_0) \tag{1.11}$$

which can be written as

$$Cos\delta_l(E) \approx \left.\frac{d\delta_l}{dE}\right|_{E_0}(E - E_0) = -\frac{2}{\tau}(E - E_0) \tag{1.12}$$

where we defined

$$\tau = \frac{2}{\left.\frac{d\delta_l}{dE}\right|_{E_0}} \tag{1.13}$$

and so the amplitude of the partial wave can be written as

$$f_l = \frac{1}{k} exp[i\delta_l(k)] Sin\delta_l(k) \tag{1.14}$$

which can be written as

$$f_l = \frac{1}{k} \frac{Sin\delta_l(k)}{Cos\delta_l(k) - iSin\delta_l(k)} \tag{1.15}$$

which can be again approximated as

$$f_l \approx \frac{1}{k} \frac{1}{-\frac{2}{\tau}(E - E_0) - i} = \frac{1}{k} \frac{-\frac{\tau}{2}}{(E - E_0) + i\frac{\tau}{2}} \tag{1.16}$$

and

$$Imf_l = \frac{1}{k} \frac{-\frac{\tau^2}{4}}{(E - E_0)^2 + \frac{\tau^2}{4}} \tag{1.17}$$

At $E \sim E_0$, partial wave $l$ is dominant and therefore cross section can be written as

$$\sigma_l{}^{tot} = \frac{\pi}{k^2}(2l + 1) \frac{\tau^2}{(E - E_0)^2 + \frac{\tau^2}{4}} \tag{1.18}$$

Now extending above formula into the compound nuclear reaction $X + a \rightarrow C^*$ and selecting the lowest partial wave, we can write cross section $\sigma_a$ as

$$\sigma_a = \frac{\pi}{k^2} \frac{\tau\tau_a}{(E - E_0)^2 + \frac{\tau^2}{4}} \tag{1.19}$$

where $\tau$ is total width and $\tau_a$ is partial width of the reaction channel $a$. The cross section of the compound nuclear reaction $X + a \rightarrow C^* \rightarrow Y + b$ is

$$\sigma_{ab} = \frac{\pi}{k^2} \frac{\tau_a\tau_b}{(E - E_0)^2 + \frac{\tau^2}{4}} \tag{1.20}$$

To experimentally test the compound nuclear reaction model, Ghoshal did an experiment with two systems $p +^{63} Cu$ and $\alpha +^{60} Ni$ to form a $^{64}Zn^*$ [7],

$$p +^{63} Cu \rightarrow^{64} Zn^* \rightarrow^{63} Zn + n \tag{1.21}$$

$$p +^{63} Cu \rightarrow^{64} Zn^* \rightarrow^{62} Zn + 2n \tag{1.22}$$

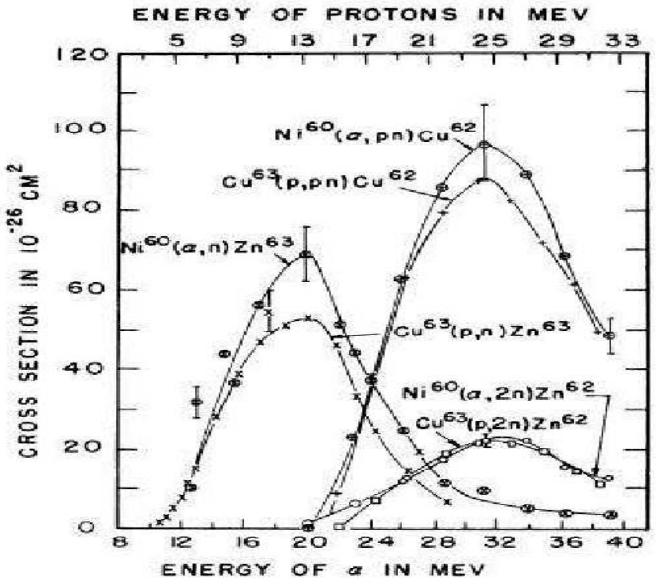


Figure 1.3: Test of compound nuclear reaction model [6].

$$p +^{63} Cu \rightarrow^{64} Zn^* \rightarrow^{62} Cu + p + n \tag{1.23}$$

and

$$\alpha +^{60} Ni \rightarrow^{64} Zn^* \rightarrow^{63} Zn + n \tag{1.24}$$

$$\alpha +^{60} Ni \rightarrow^{64} Zn^* \rightarrow^{62} Zn + 2n \tag{1.25}$$

$$\alpha +^{60} Ni \rightarrow^{64} Zn^* \rightarrow^{62} Cu + p + n \tag{1.26}$$

In this experiment, it is observed that ( see 1.3)

$$\sigma_{p,n} : \sigma_{p,2n} : \sigma_{p,pn} = \sigma_{\alpha,n} : \sigma_{\alpha,2n} : \sigma_{\alpha,pn} = \tau_n : \tau_{2n} : \tau_{pn} \tag{1.27}$$

Which is same as predicted by compound nuclear model.

## 1.2 Particle evaporation from compound nucleus

To get spectroscopic information of nuclei of light and intermediate mass regions, typically evaporation reactions have been used. In these reactions, the projectile

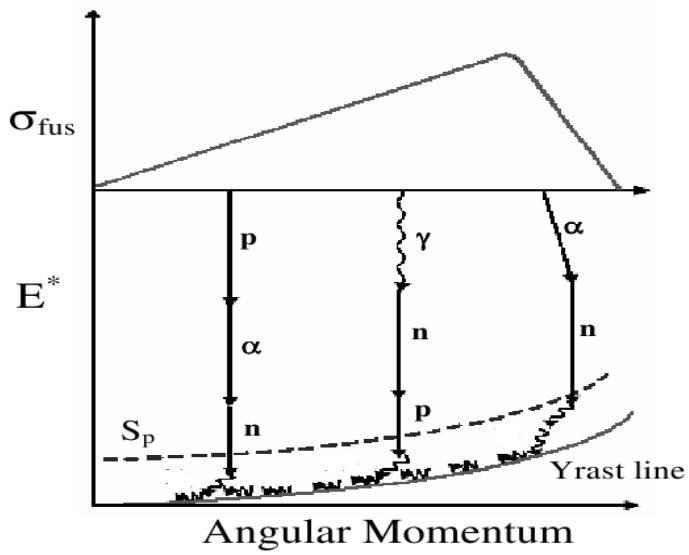


Figure 1.4: Schematic diagram showing the decay of compound nucleus.

and the target nuclei merge together to form the compound nucleus. The compound nucleus has no memory of its initial stage except for energy, momentum and angular momentum conservation. Excitation energy $E^*$ of compound nucleus can be given by the following formula

$$E^* = Q + E_{be}(1 - \frac{m_{be}}{m_{be} + m_t})) \tag{1.28}$$

where $m_{be}$ and $m_t$ are the masses of the beam ( projectile ) and the target nuclei, respectively, and $E_{be}$ is beam energy. In the above equation, energy and momentum conservations have been assumed. $Q$ is called the $Q$ value and is defined as the difference between masses of initial and final states:

$$Q = m_{be} + m_t - m_{cn} \tag{1.29}$$

where is $m_{cn}$ is mass of compound nucleus. There is no such way found which precisely predict the decay of compound nucleus, but some general feature may be found out. One of them is the emission of light particle from compound nucleus. In the beginning stage of decay of compound nucleus, light particles are emitted

isotropically in center of mass system. Because of Coulomb barrier, emission of neutron is faster than emission of charged particles ( proton, alpha ). Each emitted particle remove 4-8 MeV energy per nucleon and carry few unit of angular momentum, leaving angular momentum of residual nucleus reduced. Due to particle emission, excitation energy and angular momentum of compound nucleus keep dissipating. This particle emission continue until emission probability of particle emission and $\gamma$-ray emission become equal. Particle emission stop when excitation energy of compound nucleus become lower than particle separation energy $S_p$ ( see Fig 1.4 ). After particle evaporation, residual nucleus is left in state of high angular momentum, while its excitation energy is of the same order as the particle separation energy. Subsequently, residual nucleus decays via emission of $\gamma$-rays. At high excitation energy, density of states is larger and so many closely placed states are available. Transitions between these states create continuous background without considerably lowering total angular momentum. When excitation energy becomes enough low, the nucleus finally decays through discrete transitions between yrast states, which are widely spaced in excitation energy.

## 1.3 Decay probabilities of compound nucleus

Compound nucleus is considered to be in statistical equilibrium with respect to all degree of freedom. Spin distribution of compound nucleus is obtained from fusion cross section using strong absorption model. Particle emission from compound nucleus is calculated using Hauser-Feshbach formula [8]. Probabilities of decay of compound nucleus are estimated from statical weight of the final states and barrier penetrability for various reaction channels. Only neutron, proton, $\alpha$-particle and $\gamma$-ray emissions are included in calculations. It is found that the effect of deuteron and $^6Li$ emissions are negligible for the reactions and so not included in calculations. Level densities of the product nuclei are estimated using Fermi gas model. At low excitation energy, the parameters can be estimated empirically. Measured residue cross sections are summed over the energies of all intermediate nuclei in the

evaporation chain, also over different evaporation chains leading to the same product. Therefore statistical fluctuation is not considered. Fission process is another de-excitation mode of compound nucleus, which is important only at the highest angular momentum for the nuclei considered in this analysis. In this case, contribution of fission processes can be taken into account by a proper choice of the angular momentum range in the compound nucleus. Pre-equilibrium decay of nucleus is also possible. The contribution of pre-equilibrium is limited to forward most angle in the present case and therefore neglected. This can be justified by comparing the experimental energy distribution of the evaporation particles with corresponding theoretical prediction at backward angles.

The fusion cross section of formation of compound [9, 10] nucleus of spin $J$ and parity $\pi$ from projectile of spin $J_P$ and target of spin $J_T$ at energy $E_{cm}$ is calculated using formula

$$\sigma(J,\pi) = \frac{\pi\lambda^2(2J+1)}{(2J_P+1)(2J_T+1)} \sum_{S=|J_P-J_T|}^{J_P+J_T} \sum_{L=|J-S|}^{J+S} T_L(E_{cm}) \tag{1.30}$$

where $S = J_P + J_T$ is the spin of the compound nucleus. Integration over angular momentum is restricted due to parity selection rule

$$\pi = \pi_P \pi_T (-1)^L \tag{1.31}$$

For absorption of heavy ions, the transmission coefficient $T_L$ depends on energy and orbital angular momentum $L$, and can be estimated using Fermi distribution

$$T_L = \frac{1}{1 + exp[(L - L_0)/d]} \tag{1.32}$$

where $L_0$ and $d$ are parameters. The value of parameter $L_0$ is selected such the measured fusion cross section

$$\sigma_{cn} = \sum_{J,\pi} \sigma(J,\pi) \tag{1.33}$$

is reproduced. By selecting $L_0$ in this way, correction due to direct reaction can be included. Direct reactions are normally considered to be surface reactions. There

is no much knowledge about diffuseness constant $d$. Here, the value of diffuseness constant is obtained from Optical model potential.

The formula for particle emission probability is obtained from the inverse cross sections using reciprocity theorem [9, 10, 11]. In reciprocity theorem, rate of decay of a particle from compound nucleus is considered to be equal to that of the absorption of a particle in to the product nucleus. Inverse cross section is written in terms transmission coefficients and therefore transmission coefficient is required to calculate emission probability. The rate $R_X dE_X$ for emitting a particle $X$ from excited compound nucleus 1 to produce a product nucleus 2 is calculated using

$$R_X dE_X = \frac{\rho_2}{2\pi\hbar\rho_1} \sum_{S=|J_2-S_X|}^{J_2+S_X} \sum_{L=|J_1-S|} T_L(E_X) dE_X \tag{1.34}$$

where $E_X$, $S_X$ and $L$ is the kinetic energy, spin and orbital angular momentum of particle $X$. $\rho_1$ and $\rho_2$ are level densities of compound nucleus and product nucleus, respectively. Here transmission coefficients $T_L$ of particle x on nucleus 2 are obtained using optical model using average parameters. Spin-orbit effects are neglected. In summation over angular momentum $L$, parity conservation is taken into account. For $\gamma - rays$, we use a similar expression to calculate emission probability which is given as [12, 13]

$$R_\gamma dE_\gamma = \frac{\rho_2}{2\pi\hbar\rho_1} \sum_L \eta_L f_L(E_\gamma) dE_\gamma \tag{1.35}$$

where $L$ and $f_L(E_\gamma)dE_\gamma$ are the multipolarity of $\gamma-$ rays and energy dependent strengths, respectively. Only $E_1$, $M_1$ and $E_2$ transitions are considered in calculations. Energy dependence $f_L$ is assumed to be equal to $E\gamma^{(2L+1)}$. Here, $E\gamma^{(2L+1)}$ is considered to be the basic energy dependence for single-particle transitions. The constant $\eta_L$ is obtained from the strength of transition between low lying states using Weiss single-particle estimation. In the calculations, only branching ratios of various particles and $\gamma$-decay channels are used instead of absolute decay rates. Normalization is achieved by assuming that other decay modes are negligible.

## 1.4 Nuclear level density

Study of evaporation spectra of particles emitted from an excited compound nucleus gives useful information about the nuclear level density (NLD). Knowledge of nuclear level density in turn can provide an interesting test of different microscopic approaches of nuclear structure used to calculate NLD. Apart from this fundamental interest, level densities are important ingredients for both the statistical and pre-equilibrium models of nuclear reactions. In statistical models total level densities are required, whereas pre-equilibrium models need partial level densities (involving only restricted numbers of fermions). Even after substantial theoretical efforts it is not yet possible to have a complete microscopic solution including all known nuclear effects that can lead to a complete analytical form of NLD. The understanding of the variation of NLD over a wide range of excitation energy and angular momentum comes only from the phenomenology based semi-empirical formulations. One of such formulations, which is widely used in statistical model calculations, is based on the Fermi gas model [14].

For simple system with mass number $A$ with an excitation energy $E$, most general expression of level density is

$$\rho(E^*, A) = \frac{dN(E^*, A)}{dE^*} \tag{1.36}$$

where $N(E, A)$ is the total no of levels of nucleus with A constituents having excitation energy lower than E. For a spherical nucleus of mass number '$A$' at moderate excitation energy '$E^*$' and spin '$J$', the nuclear level density, $\rho_{int}(E^*, J)$, as predicted by the Fermi gas model [14] is given by:-

$$\rho_{int}(E^*, J) = \frac{(2J+1)}{12}(\frac{\hbar^2}{2\Im_{eff}})^{3/2}\sqrt{a} \times \frac{\exp(2\sqrt{a(E^* - E_{rot} - \Delta_P)})}{(E^* - E_{rot} - \Delta_P)^2}. \tag{1.37}$$

Where '$a$' is called the level density parameter. Here

$$E_{rot} = \frac{\hbar^2}{2\Im_{eff}} J(J+1) \tag{1.38}$$

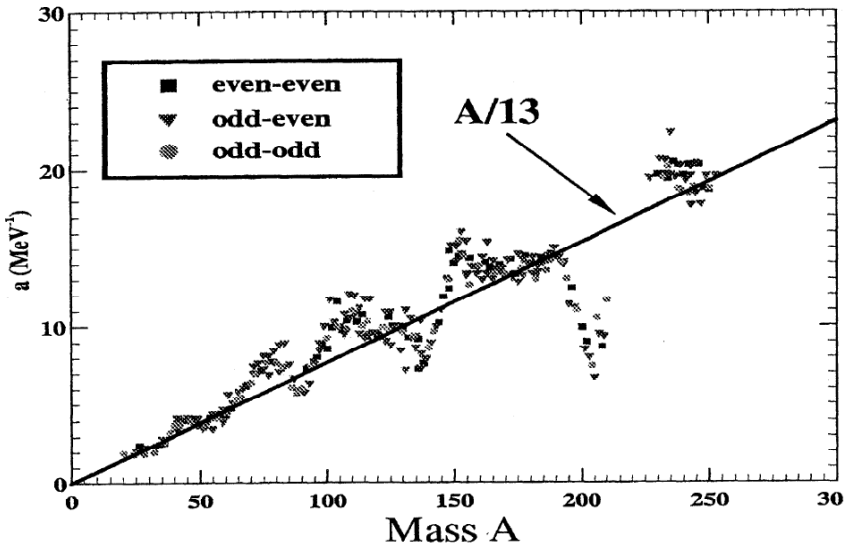


Figure 1.5: Level density parameter obtained from experimental data with theoretical predictions [15].

is the rotational energy, and

$$\Im_{eff} = \Im_0(1 + \delta_1 J^2 + \delta_2 J^4), \tag{1.39}$$

$$\Im_0 = \frac{2}{5} A^{5/3} {r_0}^2 \tag{1.40}$$

where $\Im_{eff}$ is the effective moment of inertia of the system [16]. Here $r_0$, $\delta_1$ and $\delta_2$, $\Delta_P$, $\Im_0$, and $E^*$ are the radius parameter, deformability coefficients, pairing energy, rigid body moment of inertia, and excitation energy, respectively.

Fermi gas model is independent particle model, in which it is assumed that the density of single particle states increases with the square root of kinetic energy of the particle . This model is first one which was used to obtain analytical formula of level density. In Fermi gas model, the density of single particle states for a nucleus with A fermions at Fermi level can be given as

$$g = \frac{3A}{2E_f} \tag{1.41}$$

where $E_f$ is the Fermi energy given by

$$E_f = (\frac{9\pi}{8})^{2/3} \frac{\hbar^2}{2m_0 {r_0}^2} \tag{1.42}$$

where $r_0$ and $m_0$ are the radius and mass of the nucleus at rest. Using saddle point approximation yields and above eq 1.37, one can show that

$$a = \frac{\pi^2}{6} g \tag{1.43}$$

now, if proton $Z$ and neutron $N$ of the nucleus are distinguished, then

$$a = \frac{\pi^2}{6} (g_\pi + g_\nu) \tag{1.44}$$

where $g_\pi$ and $g_\nu$ are single particle densities of proton and neutrons. The parameter $a$ is called level density parameter and can be written as

$$a = \frac{\pi^2}{4} \frac{A}{E_f} \tag{1.45}$$

where $E_f$ is given in eq 1.42. Nuclear level density parameter is found to be linear function of mass number $A$ of order ( see Fig 1.5 )

$$a \approx \frac{A}{13} \tag{1.46}$$

### 1.4.1 Shell effect on nuclear level density

Shell effect is one of the main cornerstone in mean field theory describing finite fermion systems. Shell filled with protons and neutrons in magic configuration gives extra stability compared to normally expected stability from liquid drop model. Shell effect influences fission isomers, super heavy nuclei as well as nuclear level density ( NLD ). The NLD parameter '$a$' is a function of the density of the single particle levels near the Fermi surface. Nuclear level density parameter, therefore, is influenced by the shell structure and the shape of the nucleus. Nuclear deformation due to the shell effect must be disappear at certain high excitation energy because shell effect decreases as the excitation energy increases. An excitation energy dependent the nuclear level density parameter has been introduced by Ignatyuk *et.al*, [17]

which incorporated the effect of nuclear shell structure at low excitation energy and gradually approaches to the liquid drop value at higher excitation energy. This is given as,

$$a = \tilde{a}[1 - \frac{\Delta S}{U}\{1 - \exp(-\gamma U)\}] \tag{1.47}$$

$$\gamma^{-1} = \frac{0.4A^{4/3}}{\tilde{a}}, \tag{1.48}$$

where, $\tilde{a}$ is the asymptotic value of the liquid drop NLD parameter appropriate for the excitation energy above the point where shell effects are washed out. Here $\Delta S$ is the shell correction obtained from the difference of the experimental and the liquid drop model masses and $\gamma$ is the rate at which the shell effect is depleted with the increase in excitation energy. Thermal energy is

$$U = E^* - E_{rot} \tag{1.49}$$

where $E_{rot}$ and $E^*$ are rotational energy and excitation energy of nucleus.

### 1.4.2 Effect of collectivity on nuclear level density

In recent years, several studies have been carried out to understand the dependence of nuclear level density on excitation energy, angular momentum and isospin. But one major issue yet to understand is the dependence of nuclear level density on collective excitations as a function of excitation energy. In ground state deformed nuclei, both collective rotation and vibration are possible, whereas for spherical nuclei there may be only collective vibration. At low excitation energy, collective motion gives rise to rotational and vibrational bands enhancing the level density above the single-particle value. It may be noted that, the level density prescription as given by Eq. 1.37, is based on the independent particle picture of the nucleus. However, additional contribution to NLD beyond the independent particle model may come from the collective properties (rotation and/or vibration) which involve coherent excitations of the nucleons. It can be shown that [18], if collective states

are accounted for, then the level density $\rho_{int}(E^*, J)$ is enhanced. In this situation total nuclear level density is given by

$$\rho(E^*, J) = \rho_{int}(E^*, J)K_{coll}(E^*) \tag{1.50}$$

where $K_{coll}(E^*) = K_{vib}(E^*)K_{rot}(E^*)$ is the collective enhancement factor, consisting of both vibrational and rotational contributions. $\rho_{int}$ is the single particle level density. Long range correlation cause an enhancement in single particle densities which leads to an enhancements in $a$. In deformed nuclei, main contribution to the collective enhancement of nuclear level density comes from rotational excitations [19]. The shell effect responsible for nuclear deformation disappears with increasing excitation energy. Thus at high excitation energy, rotational motion can not be distinguished from the intrinsic motion and so collective enhancement should disappear,

$$\rho(E^*, J) \rightarrow \rho_{int}(E^*, J)(i.e., K_{coll}(E^*) \rightarrow 1) \tag{1.51}$$

Bjornholm, Bohr and Mottelson [20] proposed that the temperature at which this happens can be expressed in terms the average oscillator frequency $\omega_0$ and the ground-state quadrupole deformation $\beta_2$ as

$$T_c \sim \hbar\omega_0\beta_2 \sim 40A^{-1/3}\beta_2 MeV \tag{1.52}$$

So, above the critical temperature $T_c$, nuclear level density comes back to the intrinsic value. This conditions are valid in most of the cases [21, 22].

### 1.4.3 Excitation energy and mass dependence of nuclear level density

Nuclear levels can be divided into two energy regions, namely the low energy and high energy excitations. At low energy region, levels are small in number and well separated. With increasing excitation energy, the spacing between the levels is progressively reduced. Thus, at higher excitation, the levels reach a quasi-continuum, where nuclear properties can be very well described in terms of level density of the system instead of levels [23]. From the statistical point of view, level density can

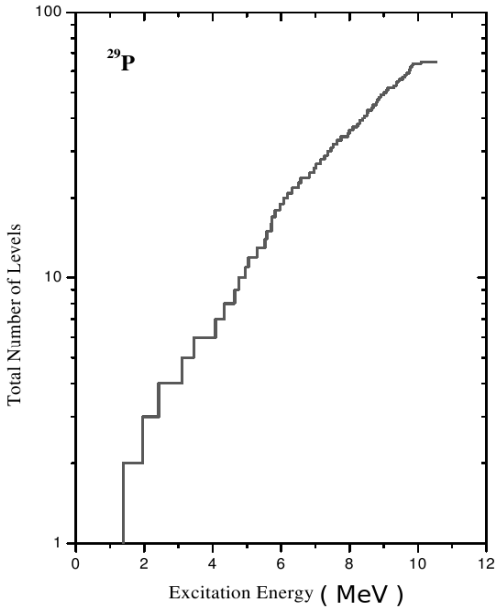


Figure 1.6: Total number of levels as a function of $E^*$ for $^{29}P$.

be used to describe nuclear properties as a function of excitation energy, angular momentum , mass number and so on. Main feature of measured total level density is that it very quickly increases with excitation energy. Rapid increase of the number of the levels with the excitation energy is shown in Fig 1.6. The total number of levels $N(E^*)$ is plotted as function of Excitation energy $E^*$ for $^{29}P$, which is a light element so its individual levels are known up to high excitation [24]. Only at low excitation energy, it is possible to separate peaks corresponding to the transitions to the discrete levels of the residual nucleus. At a few MeV excitation energy these peaks overlap and merge in continuum.

The calculations of density of states for Fermi gas model can be done by counting the number of different way, the excitation energy $E^*$

$$E^* = E - E_g \tag{1.53}$$

can be distributed among the single particle states. In above equation, $E$ and $E_g$ are total energy and total ground state energy of compound nucleus or fermion system.

Now, from the thermodynamics we know that the logarithmic derivative of state density $\omega(E^*)$ with respect to $E^*$ is related to the reciprocal of nuclear temperature $T$, by the following equation,

$$\frac{d[ln\omega(E^*)]}{dE^*} = \frac{1}{T} \tag{1.54}$$

The above equation suggests an exponential dependence of level density on the excitation energy $E^*$ [25]

$$\rho(E^*) \propto \frac{1}{T} exp(\frac{E^*}{T}) \tag{1.55}$$

When level density $\rho(E^*)$ is related to state density $\omega(E^*)$ by the relation $\rho(E^*) = \omega(E^*)/N$, $N$ being the average number of states per level. This formula is widely used to do the analysis of energy spectra of evaporated particles in statistical model and it nearly reproduces the energy dependence of yield of evaporated particles. Fischer et al. [26] and T von Egidy et al. [27] verified its adequacy up to excitation energies around the neutron binding energy. Gilbert et al. [28] verified that a constant temperature formula reproduces the experimental level densities better than the Fermi gas model at low energies.

The simplest formula of excitation energy dependence nuclear level density can be obtained by equidistant spacing model. In this model, it is assumed that independent fermions are distributed among equally spaced single particle level with level spacing $d$. In this model, expression of excitation energy and mass dependent density of states $\omega(A, E^*)$ can be given as

$$\omega(A, E^*) = \frac{\pi^{1/2} exp(2(aE^*)^{1/2})}{12a^{1/4}(E^*)^{5/4}} \tag{1.56}$$

where $a = \pi^2 g/6$ and $g = g_\pi + g_\nu$ are level density parameter and average total single fermion density, respectively. By using the expression of energy dependence of level density, relation between nuclear temperature and excitation energy can derived as

$$T = (\frac{a}{E^*})^{1/2} - \frac{5}{4E^*} \tag{1.57}$$

Reciprocal of thermodynamic temperature $t$ is defined as the first derivative of entropy $S$ with respect to excitation energy, means

$$\frac{1}{t} = \frac{dS}{dE^*} \tag{1.58}$$

In equidistant spacing model, excitation energy is related to thermodynamic temperature by

$$E^* = at^2 \tag{1.59}$$

now, using Fermi gas model formula of a, one can derive

$$T \simeq t = \frac{2}{\pi} {E_f}^{1/2} (\frac{E^*}{A})^{1/2} \tag{1.60}$$

Above formula is in agreement with excitation energy and mass dependence found in the analysis of the experimental data by using eq 1.55. This experiment was performed by Holbrow and Barschall [29].

### 1.4.4 Spin dependence on level density

Information of nuclear level density and its dependence on excitation energy, mass and spin is necessary in understanding properties of compound nuclear and in calculations of reaction cross section with in a frame work of Statistical model. In Fermi gas model, it is also possible to calculate the expression of spin dependence of nuclear level density. The dependence of level density $\rho$ on an angular momentum can be written as [30]

$$\rho(E^*, J) = \frac{2J+1}{2\sigma^2} exp\left(-\frac{J(J+1)}{2\sigma^2}\right) \rho(E^*) \tag{1.61}$$

where $\rho(E^*)$ is the level density and is written as [31, 32, 33]

$$\rho(E^*) = \frac{exp(2\sqrt{a(E^* - E_1)})}{12\sqrt{2}\sigma a^{1/4}(E^* - E_1)^{5/4}} \tag{1.62}$$

where $a$ is level density parameter and $E_1$ is best fit parameter obtained by fitting theoretical result to experimental data as shown in Fig 1.7. Spin cut-off factor $\sigma$ describe the width of the spin distribution, and $E^*$ is the excitation energy.

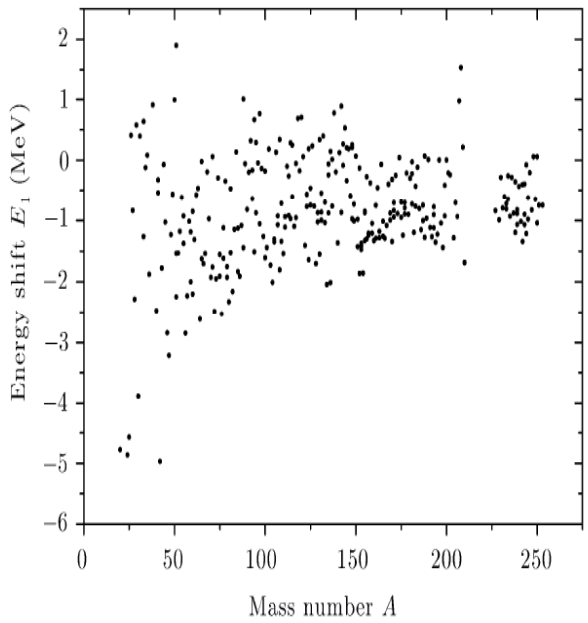


Figure 1.7: Graph of energy shift parameter $E_1$ as a function of mass number $A$.

According to Ericson [34]

$$\sigma^2 = g < m^2 > T \tag{1.63}$$

where $g$,T and $< m^2 >$ are the density of single particle states, nuclear temperature and average square of projection of spin of single particle states near the Fermi level. Quantity $< m^* > g$ can be given in terms of effective momentum of inertia $\Im_{eff}$ as

$$\sigma^2 = g < m^2 > T = \Im_{eff}\frac{T}{\hbar^2} \tag{1.64}$$

The information of nuclear level density at neutron binding energy $B_n$ and S-wave spacing $< D_{1/2^+} >$ are used to calculate spin cut-off factor [35]

$$\sigma^2 = \rho(B_n)\frac{< D_{1/2^+} >}{2} \tag{1.65}$$

and from eq 1.64, one can estimate effective momentum of inertia by using known value of $\sigma^2$ and $T$.

### 1.4.5 Measurement of nuclear level density parameter

Experimental information on nuclear level densities at lower excitation energies are obtained mainly from the counting discrete levels above the ground state and neutron resonance spacing data. Neutron resonance data contribute most extensive source of information on nuclear level densities. In such experiment the energy levels are observed at an energy just greater than the neutron binding energy $B_n$, and the number of levels is obtained by counting the resonances in a particular neutron energy interval. It is necessary that width $\tau$ of the levels must be less than the level spacing $D$ and the experimental resolution must be good enough to separate individual levels. Most important feature of the method is that it is applicable to whole range of mass number across the periodic table. Hence it is possible to study the dependence of nuclear level density on mass number. Although method of neutron resonance spectroscopy is extremely important in systematic study of nuclear level densities, it still suffers from some experimental errors. Information of nuclear level densities can also be obtained from charged particle capture resonance in the same way as described for neutron resonance capture. Charged particle resonance data are limited for light and medium nuclei due to Coulomb barrier. At higher excitation energy, most calculations of nuclear level densities are done using the Fermi gas model, to which the pairing and the shell effects are added semi-empirically.

Recently, many experiments have been carried out to investigate excitation energy and angular momentum dependence of nuclear level densities [36, 37, 38, 39]. In recent experiments, Gupta et. al. obtained the inverse level density parameter as function of angular momentum by measuring $\alpha$ evaporation spectra around $A \sim 120, 180$ at excitation energy range of $30 - 40$ MeV. They have found that value of inverse level density parameter remains almost constant with angular momentum around $A \sim 180$ in the excitation energy range of $30 - 40$ MeV [40, 41]. It was also seen that there was strong variation in inverse level density parameter as function of angular momentum around $A \sim 120$ in the excitation energy range of $30 - 40$ MeV [40, 41]. Roy et. al. and K Banarjee et. al. obtained inverse

level density as function of angular momentum by measuring the energy spectra of the evaporated neutrons, protons, and $\alpha$ particles in the reaction of $^4He$ on $^{93}$Nb and $^{58}$Ni at backward angles in coincidence with the $\gamma$ rays of various multiplicities. In this experiment, decrement in inverse level density parameter with angular momentum was observed around $A \sim 63 - 119$ in the excitation energy range of $31 - 43$ MeV [42, 43]. The decrease in the value of inverse level density parameter at higher J is indicative of the fact that NLD increases with angular momentum. Shape change at higher angular momentum based on RLDM as well as the present prescription of collective enhancement failed to explain the observed variation of NLD with J . Microscopic calculations and further investigations will be useful in order to understand the observed phenomenon in more detail.

### 1.4.6 Motivation and structure of this thesis

Main aim of present thesis was to study the neutron evaporation in energetic nuclear collisions and to design and develop required detectors and other instruments. This work is categorized in mainly two parts:

1. Experimental study of level density parameter as a function of angular momentum and excitation energy by comparing measured neutron evaporation spectra with statistical model calculation.

2. Development and characterization of organic liquid scintillator based neutron detectors for measurement of neutron energy and multiplicity.

Thesis is divided into four chapters. Chapter 1 contains physics motivation and detailed overview of the thesis work. Development and characterization of the neutron detectors are discussed in chapter 2. Complete study of the neutron evaporation in reactions $^4$He + $^{181}$Ta, $^4$He + $^{165}$Ho and $^4$He + $^{197}$Au are described in chapter 3. Finally, summery and conclusion of present thesis are presented in chapter 4.

# Chapter 2

# DETECTOR DEVELOPMENT

## 2.1 Introduction

Organic liquid scintillator based detectors are widely used to detect fast neutrons because of their good response to neutrons, high detection efficiency, good energy resolution, superior time resolution and n - $\gamma$ discrimination properties. Recently, organic liquid scintillator(BC501A) based neutron detector array is being developed for neutron spectroscopy at Variable Energy Cyclotron Centre, Kolkata. Construction of such an array needs detailed simulation of the properties of individual detector like detection efficiency, neutron response function, etc. Many standard computer codes like CECIL [44], NRESP [45], SCINFUL [46], FLUKA [47, 48], MCNP [49], etc. are developed in the past to estimate various properties of neutron detector having certain types of complex geometries. In recent time, GEANT4 [50](toolkit for simulating the passage of particles through matter ) is being extensively used by the nuclear and high energy physics community because of its versatile capability of large scale, comprehensive simulation of the experimental situations involving complex combination of different types of detectors over a very wide energy range. The accuracy of the simulation depends on (a) proper modeling of the processes involved, and (b) correctness of the data libraries used for the simulation; so, it is important to critically evaluate the performances of the processes in general, and, the data libraries in particular, by comparing with exper-

imental data. The pulse-height response of the detector, which is experimentally measurable, is an important tool to directly check the correctness of the simulation process as a whole. Here, the purpose of this work is to do comprehensive study of neutron response functions of scintillator detector for neutron energies up to 20 MeV. GEANT4 simulated responses were compared with experimentally measured responses. Mono-energetic neutron response functions have been simulated with the GEANT4 toolkit version 4.9.2 using neutron cross-section data library G4NDL3.14. G4NDL3.14 is the recently updated high precision data library containing data largely from ENDF/B-VI library [51]. Simulation of mono-energetic neutron response functions using standard FORTRAN code NRESP7 has also been presented along with the experimental and GEANT4 results for comparison. In the following sections, the detailed description of neutron detector development is given.

## 2.2 Neutron detection

Neutron has no charge and therefore it cannot interact with matter by means of Coulomb force. Due to this, neutrons cannot be detected directly. Neutrons are always detected through nuclear reactions that results in creation of energetic charged particles (such as p, and alpha) which can in turn be detected by radiation detectors. The cross - sections for neutron interactions in most materials is a strong function of neutron energy , hence different techniques have been developed for neutron detection in different energy regions.

### 2.2.1 Slow neutron detection

Neutrons are called slow if their energies are below the cadmium cutoff of about 0.5 eV. Neutrons of these energies are detected via nuclear conversion reactions, for example ( n, alpha ) or ( n, p ) reactions. All common techniques used to detect

slow neutrons result in heavy charged particles [52]:

$$\text{target nucleus} + \text{neutron} = \left\{ \begin{array}{l} \text{recoil nucleus} \\ \text{proton} \\ \text{alpha particle} \\ \text{fission fragment} \end{array} \right\} \tag{2.1}$$

The energy of the detected neutron is small compared to the Q-values of these reactions, the reaction products carry away an energy corresponding to the Q-value. This means that the information on the neutron energy is lost in these reactions. The three conversion reactions commonly used in detectors are:

$$^{10}B + n \longrightarrow \left\{ \begin{array}{l} ^{7}Li^{*} + \alpha,\ 2.310 \text{ MeV ( excited state, 94\%)} \\ ^{7}Li + \alpha,\ 2.792 \text{ MeV ( ground state, 6\%)} \end{array} \right\} \tag{2.2}$$

$$^{6}Li + n \longrightarrow^{3} H + \alpha,\ 4.78 \text{ MeV} \tag{2.3}$$

$$^{3}He + n \longrightarrow^{3} H + p,\ 0.764 \text{ MeV} \tag{2.4}$$

The energy from the reaction is shared by the two reaction products, the alpha particle (or proton) and the recoil nucleus, according to conservation of momentum and energy. The products alpha and proton are detected. The thermal neutron cross sections for these three cases are, 3840 barns, 940 barns and 5330 barns respectively [52].

The BF3 counter ( proportional ) is commonly used for thermal neutron detection since enriched $^{10}$B in BF3 gas is easily available. $^{3}$He is an expensive gas and no compounds of Li are easily available as a gas for proportional counters. The $^{6}$Li ( n, alpha ) reaction is usually used in scintillators. One can use lithium iodide, which is chemically similar to sodium iodide. Due to the density of enriched $^{6}$LiI(Eu) crystals, a 10 mm thick detector is almost 100% efficient for neutrons ranging from thermal energies up to about 0.5 eV. Lithium is also incorporated in scintillating glass matrices. Lithium glass scintillators are used in time of flight measurements due to their relatively fast time response of less that 100 ns. This type of detector, however, is more commonly used in the detection of neutrons with intermediate energies.

### 2.2.2 Fast neutron detection technique

In principle, the nuclear reactions used for the detection of slow neutrons can be used for fast neutron also; however, the cross-sections for these reactions decrease rapidly with increasing neutron energy. Therefore, the detectors mentioned earlier are very inefficient if they are used for fast neutrons. But the slow neutron detectors can be surrounded by hydrogen containing material that moderates the neutrons down to energies where the detection efficiency is high. This moderation is done by elastic scattering and the neutron can be slowed down most effectively by hydrogen nuclei. Polythene and paraffin are the most common moderators. The detection efficiency of a moderator detector combination will depend on the neutron energy and thickness of the moderator. Moderator based detectors are slow and cannot be used for time measurements.

**Detectors based on fast neutron scattering**

The most common method to detect fast neutron (neutron energy 0.1MeV - 100MeV) is based on elastic scattering of neutron on light nuclei, resulting in a recoil nucleus. Transfer of the energy depends on the atomic mass of target nucleus as well as angle of scattering. By using conservation of energy and momentum, recoil energy ($E_R$) of scattered nucleus can be calculated(non relativistically) as [52]

$$E_R = \frac{4A}{(A+1)^2} E_n \cos^2\theta \tag{2.5}$$

where $A$ is mass number of recoil nucleus, $E_n$ is kinetic energy of incoming neutron and $\theta$ is scattering angle of recoil nucleus in laboratory frame as shown in Fig 2.1. From the equation 2.5, it is clear that kinetic energy transferred to recoil nucleus increases as mass of the recoil nucleus decreases. It is also found from eq 2.5, that the kinetic energy of the recoiling nucleus varies from zero for grazing collision to finite maximum value of $E_n \frac{4A}{(1+A)^2}$ for a head-on collision. In head-on collision ($\theta = 0$ ) of neutron with hydrogen (A = 1), all kinetic energy of neutron can be transferred to recoil proton in single collision, while head-on collision of neutron with $^{12}C$, maximum fraction of energy transfer is 0.28 only.

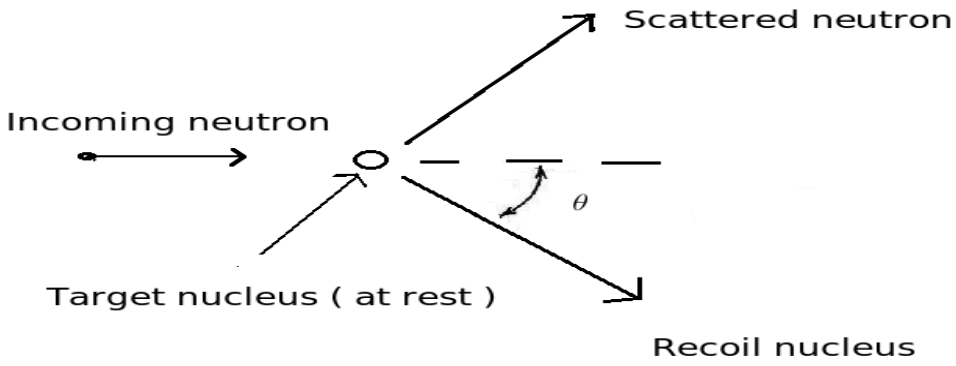


Figure 2.1: Elastic scattering of neutron in laboratory frame.

For this reason, hydrogen finds wide spread use as a detector material in recoil detection method. For the same reason, organic scintillators which contain mostly hydrogen and $^{12}C$, are used for detection of fast neutron. For measuring the energy of fast neutron, time of flight technique is generally used. At VECC, a large number of time of flight type detectors have been developed. In the present thesis, a detail characterization ( pulse height response ) of a prototype detector has been done and will be presented in this chapter. In the following, the principle and characteristics of scintillator detectors will be described in detailed.

### 2.2.3 Basic principle of scintillator detectors

Scintillation is a process, in which, light is emitted due to de-excitation of atoms or molecules of scintillator, which are excited due to energy loss of the ionizing particle. The fact that certain materials scintillate on the passage of ionizing radiation forms the basis of a scintillation detector. Scintillation emission depends on a sequence of secondary processes but still maintains some proportionality of the number of emitted photons to the deposited specific energy loss. For example, one scintillation

photon requires, on an average, an energy deposition of about few eV. The near constancy of the energy required to produce one scintillation photon forms the basis of energy measurements with scintillation detectors. A scintillation detector essentially consists of a scintillator optically coupled to a photomultiplier tube ( PMT ).

When an ionizing radiation fall on Scintillator, it excites the atoms or molecules of the scintillator which de-excites by emitting photons. A fraction of these emitted photons are collected by the photocathode of the photomultiplier tube which liberates photoelectrons. They are further amplified by dynodes of the PMT, giving rise to a large current pulse passing through a load resistor. The ideal scintillation materials should have the following properties:

1. It should convert the kinetic energy of the charged particle into scintillation light with high efficiency.

2. The conversion should be linear.

3. The medium should be transparent to its scintillation radiation.

4. Decay time of the induced luminescence should be short for the generation of fast signal.

5. The index of refraction for the material should match with the glass for efficient coupling of light to the photo cathode.

Since no single scintillation material has all the desired properties, depending on specific applications one chooses a scintillator. For example, for gamma ray energy spectroscopy, inorganic alkali halide, and, in particular thallium activated sodium iodide are used. They have better light output and linearity but are relatively slow. For fast timing, organic scintillators are preferred. Organic scintillators(liquid and plastics) are also preferred for $\gamma$-ray spectroscopy and fast neutron detectors.

### 2.2.4 Classification of Scintillation Materials

Scintillators are mainly classified into two groups. i) Inorganic Scintillators (e.g. NaI(Tl), CsI(Tl) etc.) ii) Organic Scintillators (e.g. Anthracene, Transstilbene, plastic, liquid etc.)

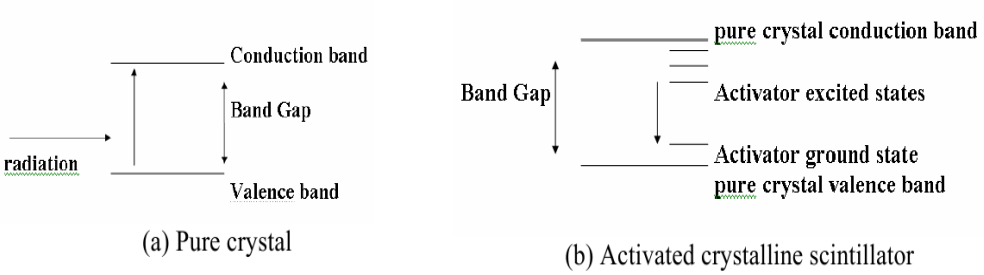


Figure 2.2: Energy band structure in inorganic crystal.

**Scintillation mechanism in Inorganic crystal with activators:**

In inorganic scintillator, scintillation requires impurity to be added to the crystal to modify the band structure. In the pure inorganic crystal, absorption of the energy of ionizing radiation excites electron from valence band to conduction band by crossing the band gap. But due to the higher width of band gap in pure crystal, de-excitation of an electron from conduction band to valence band does not result into emission of photon within the visible range which is acceptable to the PMT. Small amount of impurities called activators are therefore added to the pure crystal. Activators create special states in the forbidden gap of the pure crystal, so the energy levels of the crystal become effectively narrower than those of the pure crystal as shown in Fig 2.2. Now, photons will be emitted within visible range when charged particle will pass through the inorganic scintillator.

**Scintillation Process in Organic Materials**:

The mechanism of scintillation in organic scintillator is different from that in inorganic scintillator. In organic scintillators, the scintillation occurs because of the electronic transitions in the energy levels of a single molecule therefore scintillation is observed in all solid, liquid and gaseous states. The organic scintillators are usually aromatic hydrocarbon compounds containing linked or condensed benzene-ring structures. In aromatic hydrocarbons there are two types of chemical covalent bonds that are important, the $\sigma$ bond and the $\pi$ bond. A carbon atom ready for

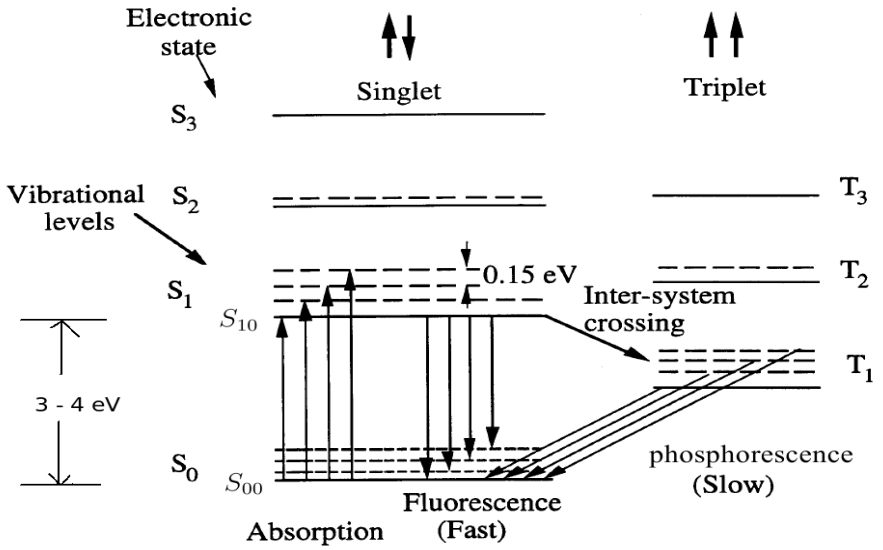


Figure 2.3: Typical energy levels of organic molecules

binding will have an electron configuration of $1s^2 2sp^3$, meaning one valence electron in an s orbital and three valence electrons in p orbital. Since the s electron orbital is spherically symmetric it will always form axially symmetric $\sigma$ bonds while the p electron orbital (orbital with two lobes)can form either axially symmetric $\pi$ bonds or mirror symmetric $\pi$ bonds. The $\sigma$ bonds are the normal regular tetrahedron bonds of carbon and they do not contribute to the luminescence of the liquid, whereas the $\pi$ bonds cause double and triple bonds and are responsible for the luminescence. In the aromatic hydrocarbons there are several of these p orbital that make up a delocalized $\pi$ system that can be modeled as free electrons orbiting the molecule. From the free electron model of the $\pi$ electrons (p electrons in a delocalized $\pi$ system) moving in a one-dimensional circle, the $\pi$ electron will have a certain ground state and a number of excited states. The $\pi$- electronic energy levels of an organic molecule are shown in Fig 2.3.

In the Fig 2.3, the energy levels of spin singlet states and spin triplet states are shown as $S_0$, $S_1$, $S_2$, $S_3$... and $T_1$, $T_2$, $T_3$ ...respectively. The energy spacing between $S_0$ and first excited state $S_1$ is $\sim$ 3 - 4 eV at room temperature. The triplet states

are usually lower in energy than their singlet counterparts. Each of these levels are further divided into vibrational energy levels as $S_{00}$; $S_{01}$; : : : ; $S_{10}$; $S_{11}$; : : : and $T_{10}$; $T_{11}$; : : : ; $T_{20}$; $T_{21}$; : : :. Typical spacing of these vibrational levels is of the order of 0.15eV. This kind of structure gives rise to three types of light that can be produced in the organic scintillator: fluorescence, phosphorescence and delayed fluorescence.

Since the spacing between vibrational state is large compared with the average thermal energies ( 0.025 eV), most of the molecules are in $S_{00}$ state at room temperature. When charged particle passes through organic scintillator, kinetic energy is absorbed by the molecules, and electrons are excited to the upper levels. The higher singlet electronic states(viz. $S_2$, $S_3$ etc.) which are excited, de-excite quickly (picoseconds) to $S_1$ state through radiationless transitions (internal conversion). The States such as $S_{11}$, $S_{12}$ that have extra vibrational energy and are not in thermal equilibrium with neighboring molecules, quickly lose that vibrational energy. Hence, within a very short period of time, a population of excited molecules in $S_{10}$ state is produced due to excitation process. Scintillation light, prompt fluorescence, is emitted in transitions between $S_{10}$ and the ground state $S_{0x}$. Intensity of scintillation at time $t$ after excitation is given as

$$I = I_0 e^{-t/\tau} \tag{2.6}$$

where $\tau$ is the decay time of level $S_{10}$. For most of the organic scintillator, decay time is in order of few nanosecond therefore these type of scintillators are called fast-scintillators.

It is also possible that electron from $S_{10}$ levels first decay to the triplet states $T_1$ ( called inter system crossing ) and then decay to $S_{00}$ by emitting light. Since the life time of the state $T_1$ is much longer ( in order of millisecond ) than that of $S_{10}$ ( in order of nanosecond ), such emission of light is called delayed light emission or phosphorescence and do not contribute to the pulse produced by prompt fluorescence.

However, instead of a transition to $S_0$, some of the molecules can be excited back to $S_{10}$ and then decay to $S_0$, which is called delayed fluorescence. Decay time for this delayed fluorescence case is $\sim$ 100 - 500 ns. The scintillation light is thus superposition of two or more exponential decay components with different decay time constants. Delayed fluorescence constitutes the slow component of the scintillation light and is mainly responsible for the neutron gamma discrimination property of liquid scintillator.

### 2.2.5 Pulse shape discrimination

Liquid scintillator detectors are extensively used to detect neutrons in mixed field of neutron (n) and $\gamma$-ray due to their excellent pulse-shape discrimination (PSD) properties to separate neutron events from $\gamma$ events [53, 54, 55, 56, 57, 58]. As described in previous section, light emission from the scintillator contains two components, a prompt fluorescence which is fast component and a longer-lived component known as delayed fluorescence which is slow component. Compared with the prompt decay time of a few nanoseconds, the slow component have typical decay time of several hundred nanoseconds. PSD technique utilizes the fact that the decay fraction of the slow component depends on the type of ionizing particle which cause scintillation. Ionizing particles having higher ionizing power creates higher concentration of excited molecular states, so the probability of $S_{10}$ state of one molecule interact with $T_1$ state of another molecule increases. So, the slow component in light emission increases as the ionizing power increases as shown in Fig 2.4.

### 2.2.6 Pulse-height response of Organic liquid scintillator

As discussed in previous section, neutron looses energy in scintillator mainly due to elastic scattering with proton. Neutron scatters isotropically from proton in center of mass frame therefore energy distribution (dN/dE) of recoil proton is step function from zero to initial neutron energy [59]. For electron, light output(L) is linearly related to deposited energy(E) but for proton and carbon, light output is not linearly related to deposited energy [59]. For proton, $L$ = k $E^{3/2}$, where k is

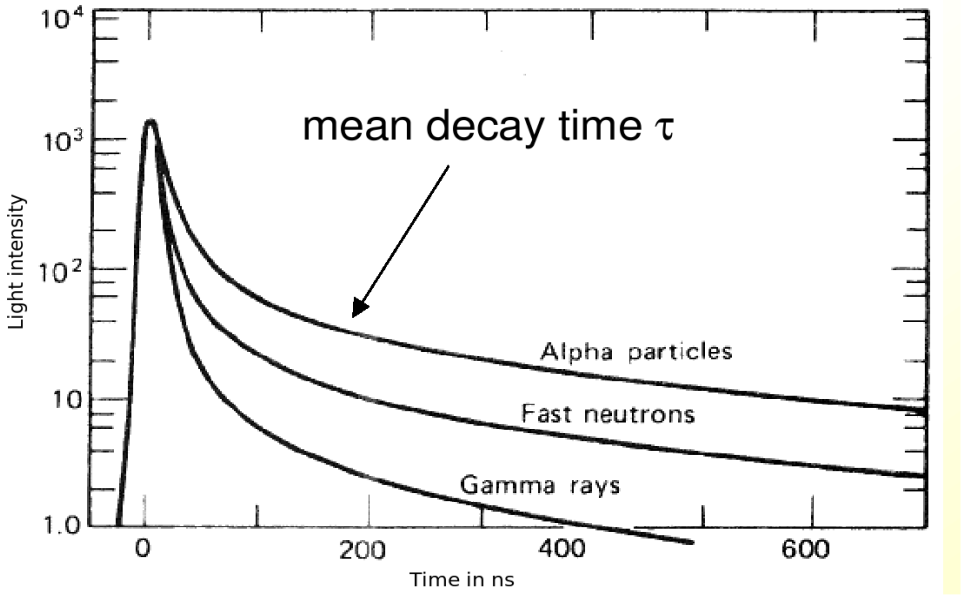


Figure 2.4: Scintillation pulses in stilbene when excited by different type of radiation [60].

constant. Thus, pulse-height distribution (dN/dL) due to proton is given as

$$\frac{dN}{dL} = \frac{dN}{dE}\frac{dE}{dL} = \frac{dN}{dE}\frac{1}{\frac{2}{3}kE^{1/2}} = (constant)L^{-1/3} \tag{2.7}$$

Fig 2.5 shows energy distribution of recoil proton and effect of nonlinear light output function on pulse-height distribution function.

Below incident neutron energy ∼8 MeV, effect of carbon on pulse-height distribution is negligible, since maximum 28% of incident neutron energy can be transferred to carbon due to elastic scattering. Above ∼8 MeV neutrons, nuclear reactions $^{12}$C(n,$\alpha$)$^{9}Be$ and $^{12}$C(n,n')$^{9}3\alpha$ affect the lower part of the pulse-height spectrum due to lower scintillation efficiency of alpha particles than that of proton [61].

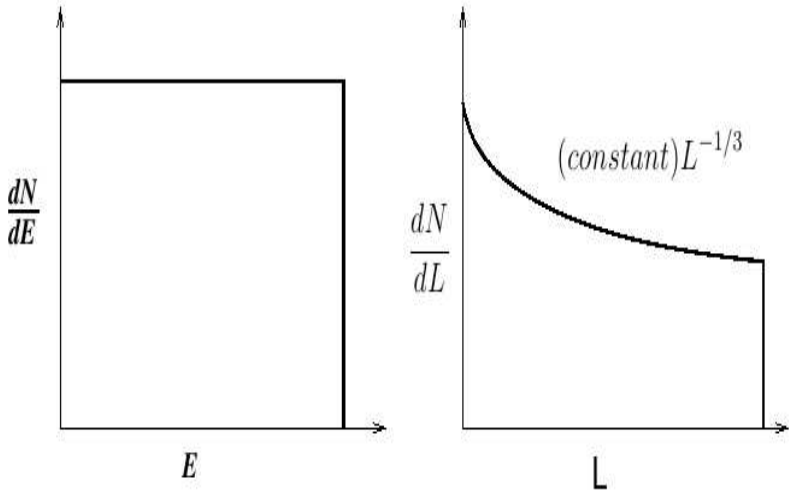


Figure 2.5: Energy distribution(left) and pulse-height distribution(right) of recoil proton.

## 2.3 Characterization of Organic liquid scintillator type neutron time of flight detector

Organic liquid scintillator(BC501A) based neutron TOF detector array is being developed for neutron spectroscopy at Variable Energy Cyclotron Centre, Kolkata. The Time-of-flight (TOF) technique is a method by which the kinetic energy of a neutron is determined, by measuring the time it takes to travel a known distance. Liquid scintillator based detectors are widely used for neutron energy measurement using time of flight technique due to their properties like relatively high light output, good detection efficiency, fast decay time and excellent neutron gamma (n - $\gamma$) discrimination. A detail characteristics of such detectors have been done in the present thesis work, and will be presented in the following sections.

### 2.3.1 Properties of The BC-501A liquid scintillator

It is found that among the available scintillators, BC501A ( manufactured by M/S Saint - Gobain )( or equivalently NE213 ) has very good pulse shape discrimination

capability and good time resolution. Therefore it is widely used for neutron detection. This is a scintillator liquid based on xylene or dimethylbenzene, $C_6H_4(CH_3)_2$. Xylene is flammable with a flash point ( the temperature where it can form an ignitable mixture in air ) of 24 degrees Celsius and poisonous since it can cause neurological damage at high exposures. The liquid BC-501A has a light output that is about 78% of anthracene, a maximum emission wavelength of 425 nm and a hydrogen to carbon ratio of 1.287. It has three decay components with 3.16 ns, 32.3 ns and 270 ns. The 270 ns component is mainly responsible for the pulse-shape discrimination (PSD) properties.

### 2.3.2 Fabrication of neutron detector

Four different sized liquid scintillator detectors (length $\times$ diameter : 1.5" $\times$ 5" , 3" $\times$ 5" , 5" $\times$ 5" , 7" $\times$ 5" ) were fabricated at Variable energy cyclotron center (VECC). Main purpose of fabrication of different sized detectors were to study the effect of detector dimensions on detection efficiency and other properties of detector. The detector cells, were fabricated using 3-mm-thick stainless steel cylindrical container filled with xylene-based liquid scintillator BC501A. Internal walls of the cells were white painted to achieve better light collection. To remove any dissolved oxygen present in the liquid, after filling the detector with liquid scintillators, detector cells were thoroughly flushed with dry nitrogen gas of purity ( 99.999% ) for sufficient time [62]. A small expansion chamber( 10% of the detector volume ) was coupled to each detector cells which took care the thermal expansion of the liquid. The Scintillator cells were sealed with 6-mm-thick pyrex glass, and finally coupled with photomultiplier tube( of diameter 5" )( model:9823B; Electrontube Ltd. ). The photomultiplier tubes were provided with $\mu$ -metal shield to protect them from magnetic field. The neutron detector cells are shown in Fig 2.6.

### 2.3.3 Measurement of PSD

Quality of pulse shape discrimination is measured in terms of Figure Of Merit (FOM), which is given by

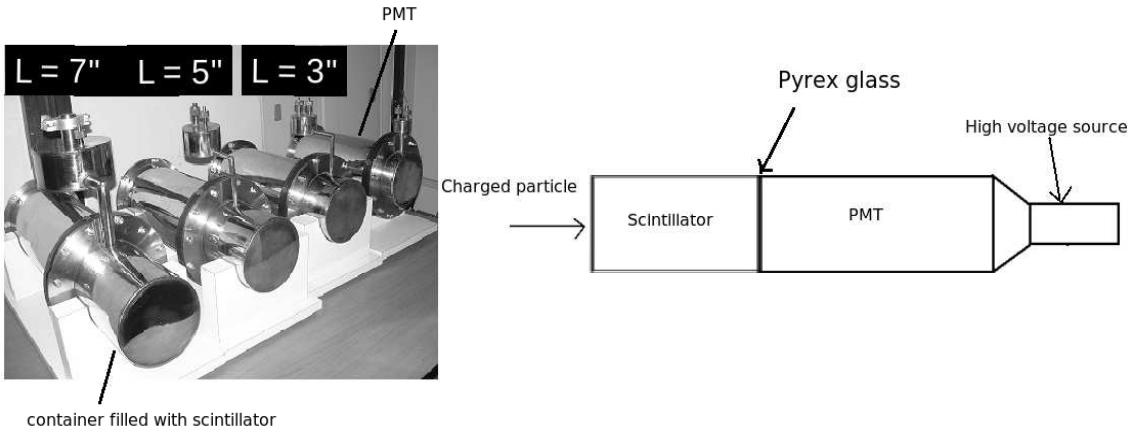


Figure 2.6: Schematic diagram ( right ) and picture of organic liquid scintillator detector( left ).

$$M = \frac{\Delta}{\delta_n + \delta_\gamma} \tag{2.8}$$

where $\Delta$ is separation between neutron peak and $\gamma$ peak, and, $\delta_n$, $\delta_\gamma$ are full width at half maximum (FWHM) of neutron peak and $\gamma$ peak, respectively. Figure of merit of scintillator detectors of size 5" diameter $\times$ 5" length and 5" diameter $\times$ 7" length was measured using $^{241}AmBe$ source. Americium emits $\sim$ 5 - 6 MeV alpha and $\gamma$- rays with different energies between 0.02 - 0.1 MeV and beryllium has large cross-section for nuclear reaction

$$^{9}Be_4 +^{4} He_2 \rightarrow^{13} C^* \rightarrow^{12} C_6 +^{1} n_0 + \gamma \tag{2.9}$$

The Q value of this reaction is 5.7 MeV. Due to above reaction, $\gamma$-rays of energy 4.44 MeV and neutrons up to energy 13 MeV are emitted. Hence, in this experiment, $^{241}AmBe$ acts as source of neutron as well as $\gamma$ ray. Experimental setup to measure Figure Of Merit is described in next section. Neutron and $\gamma$-ray events are very well separated for both the detectors as seen from Fig 2.7. However, value of M decreases with increase in the detector length due to higher reduction in light collection by PMT ( since dimensions of PMT were same in both the detector ) and higher time

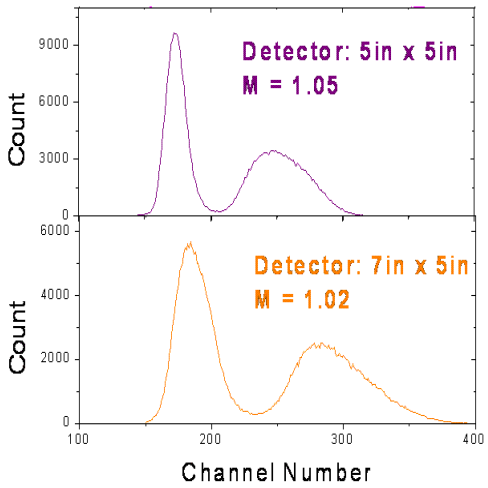


Figure 2.7: Pulse shape discrimination spectrum for two different sized liquid scintillator detectors.

spread in arrival of light at PMT.

## 2.4 Measurement and simulation of pulse-height response

Pulse-height response functions of mono-energetic neutrons from continuous neutron energy field have been measured using BC501 organic liquid scintillator based neutron time of flight detector. Experimental setup and electronics setup used in this experiment are discussed in following two sections.

### 2.4.1 Experimental setup

A schematic diagram of the experimental setup is shown in Fig 2.8. The setup consisted of a thin-walled (3 mm stainless steel) reaction chamber, a liquid scintillator (BC501A) TOF neutron detector (size 7" $\times$ 5") [63], and, an array of 50 $BaF_2$ $\gamma$-ray multiplicity detectors [64]. The $^{252}$Cf neutron source (100 $\mu$Ci.) was placed at the centre of the chamber and the neutron detector was kept at a distance of 150 cm

from the centre. $BaF_2$ $\gamma$-ray multiplicity detectors were divided into two blocks, each containing 25 detectors; one block each was placed on the top and at the bottom of the chamber (see Fig. 2.8), respectively, in closest possible vicinity symmetrically around the centre of the chamber (source position), for highest possible solid angle coverage (56% of $4\pi$ solid angle). The $BaF_2$ detectors, having fast response which allows sub-nanosecond timing, were used to generate time reference for the TOF measurement by detecting, as efficiently as possible, the prompt $\gamma$-rays emitted from the $^{252}$Cf source. By measuring the time difference between the $BaF_2$ signal and neutron detector signal, the Time-of-flight spectra of neutrons were archived. Pulse shape discrimination (PSD) method was used to separate $\gamma$-ray events from neutron events, and mono-energetic neutron response was extracted from continuous energy neutron spectrum by selecting appropriate TOF-windows in the TOF spectrum.

### 2.4.2 Electronics setup

The layout of the electronics and data acquisition setup is shown in Fig. 2.9. Amplified Signals of all $BaF_2$ detectors were fed to constant fraction discriminator (CFD) to generate timing signal. Main task of CFD is to generate logic signal from the analogue signal of fast amplifier without losing timing information. Logic OR of all CFD timing outputs of $BaF_2$ detectors was used as start input of a time-to-digital converter (TDC) for neutron TOF measurement. Neutron detector signal was directly fed to a multichannel pulse shape discriminator [65], which generated CFD timing, zero cross-over time (ZCT) and pulse-height (PH) outputs simultaneously. Delayed CFD timing output of neutron detector was used as stop signal of TDC. The ZCT and PH signals of the neutron detector were digitized using analog to digital converter (ADC). The PH, ZCT and TOF data were finally collected on event by event basis using a VME-based online data acquisition system [66].

Measured TOF spectrum and ZCT vs. PH two dimensional scatter plot for neutrons and $\gamma$-rays emitted from source $^{252}Cf$ are shown in Fig. 2.10(a and b). From the ZCT vs PH plot, it is seen that the neutron events are very clearly sepa-

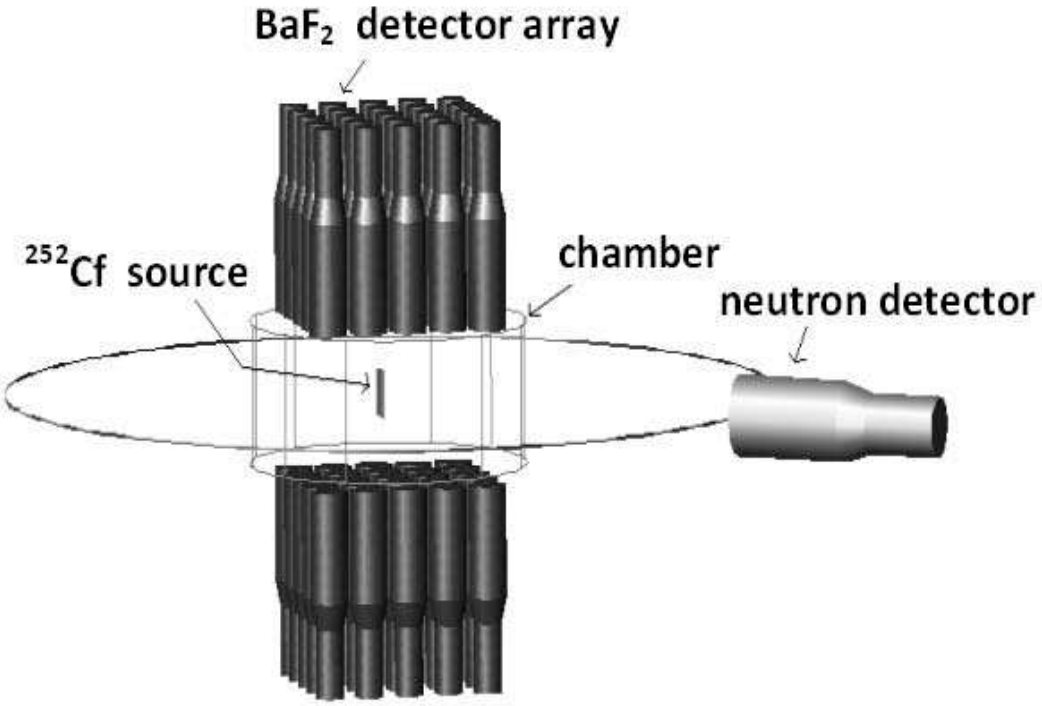


Figure 2.8: Experimental setup to measure pulse height response of neutron using time-of-flight method.

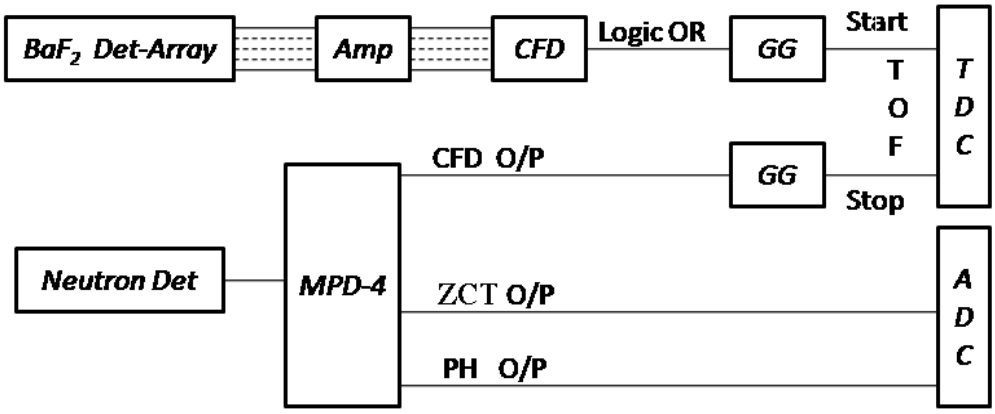


Figure 2.9: Block diagram of the electronics setup to measure pulse height response of neutron using time-of-ight method.

rated from the $\gamma$ events and there is no overlap between the two. Genuine neutron events were selected using a two dimensional gate over the neutron band (as shown in Fig. 2.10) in the ZCT vs. PH plot. PH spectrum of mono-energetic neutrons was then extracted from pure neutron PH spectrum by selecting a TOF window corresponding to the neutron energy. TOF window for mono-energetic neutron was calculated using non-relativistic equation $E = 1/2mv^2$. The TDC calibration ($\sim$50 ps/channel) was measured several times during the experiment using time calibrator to convert channel number of TOF spectrum into flight time of neutron. $\gamma$ peak in TOF spectrum was considered as reference time for neutron time-of flight measurement. Measured spectra of neutron of energy 2 MeV is shown in Fig. 2.10.

The PH spectrum was calibrated using the Compton edges of two mono-energetic $\gamma$-sources ($^{22}Na$ and $^{137}Cs$).

### 2.4.3 GEANT4 simulation of pulse-height response

We have done the simulation using a GEANT4 toolkit to estimate pulse height response of BC501A Organic Scintillator detectors. GEANT4 is software package used for full Monte Carlo simulation of detectors used in high energy physics, nuclear and accelerator physics. GEANT4 simulation uses physics models which are well tested by scientists and engineers of GEANT4 collaborators. GEANT4 user creates a detector simulation program using classes provided by GEANT4 to construct detector geometry, to add physics process and to do required calculations for his/her own detector setup.

#### Detector construction in geant4

The simulation includes full mechanism of the light production inside the detector, wall effect, detector resolution and non-linear light response for all secondary charged particles. By using G4Tube and G4Material classes, a tube made of material BC501A was created to construct liquid scintillator detector of sized ( $length \times diameter$ : 7" $\times$ 5" ) as shown in Fig 2.11. To add wall effect, a container was placed around BC501A material. Photomultiplier tube was ignored.

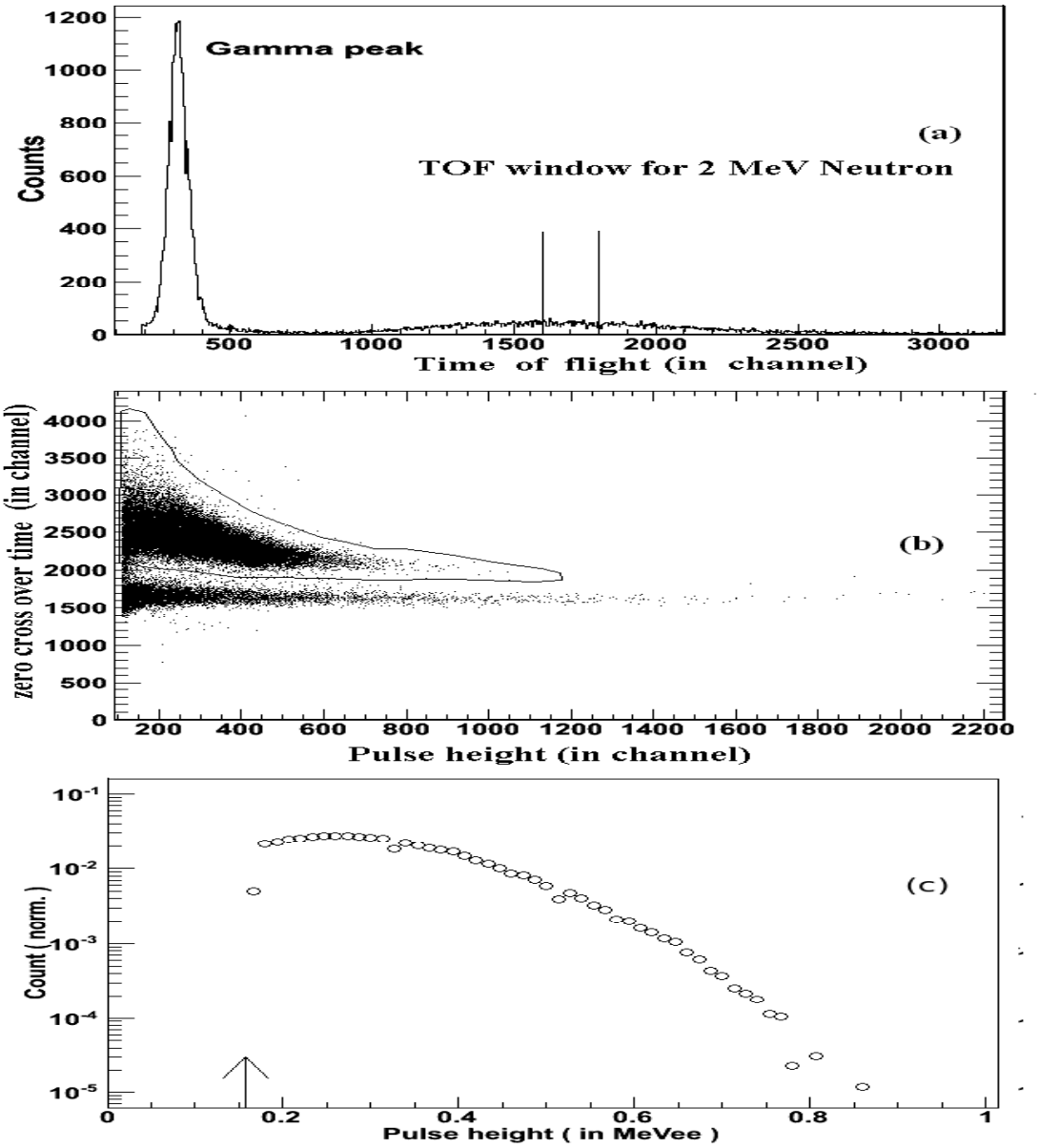


Figure 2.10: (a) TOF spectrum and (b) two-dimensional plot of ZCT vs. PH for Cf source (c) experimental pulse height spectrum for 2 MeV neutrons. Detector threshold is shown by arrow.

**Physics models**

All relevant physical processes for $\gamma$-rays and neutrons in the energy range in question were included in the simulation. For $\gamma$-ray interactions, the data file G4EMLOW version 6.2, containing cross-sections for low energy electromagnetic processes, was used. For neutron, cross section data library G4NDL3.14, in which NeutronHP models of Elastic, Inelastic, Capture and Fission process are incorporated, have been used. The NeutronHP models in GEANT4 cover the energy range up to 20 MeV for the neutron scattering [50].

**Neutron beam**

It is seen that the shape of neutron response function is strongly influenced by small variation of neutron energy; hence, to compare the simulated spectrum with spectrum measured using TOF technique, energy resolution of TOF technique was also included in the simulation by generating a neutron pencil beam of energy having a Gaussian distribution with centroid at E and FWHM equal to the corresponding $\triangle E$. $\triangle E$ was selected by calculating time of flight resolution given by equation

$$\left(\frac{\triangle E}{E}\right)^2 = \left(\frac{2\triangle\tau}{t}\right)^2 + \left(\frac{2\triangle l}{l}\right)^2 \tag{2.10}$$

where $\triangle\tau = 0.05$ ns is the time resolution of detector, $t$ is neutron flight time , $l = 150$ cm is neutron flight path, $\triangle l = 17.78$ cm is the flight path spread due to the length of detector used. Calculated Time of flight resolution were also directly verified by measuring width of $\gamma$-peak in TOF spectra.

**Calculation of total light output**

As discussed earlier, energy deposited by charged particles in the scintillator need to convert in to fluorescent light energy. In GEANT4 simulation, the energy deposited in detector was converted in to light output using Cecil's prescriptions [67] as described below.

$$L(E_p) = 0.83E_p - 2.82(1 - \exp(-0.25{E_p}^{0.93})) \tag{2.11}$$

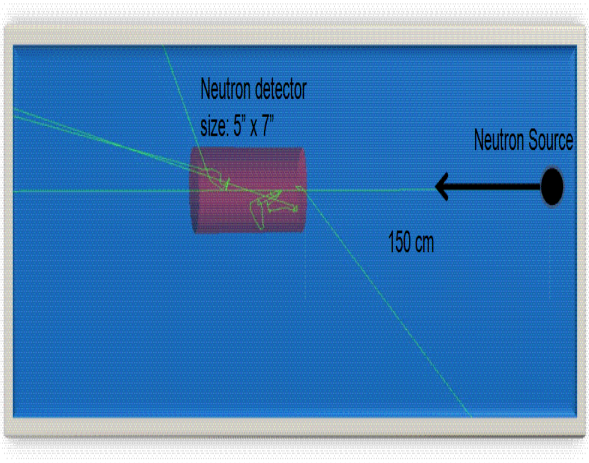


Figure 2.11: Visualization of setup used for pulse-height simulation in Geant4.

$$L(E_\alpha) = 0.41E_\alpha - 0.59(1 - \exp(-0.065{E_\alpha}^{1.01})) \tag{2.12}$$

$$L(E_{Be}) = 0.0821E_{Be} \tag{2.13}$$

$$L(E_B) = 0.0375E_B \tag{2.14}$$

$$L(E_C) = 0.017E_C \tag{2.15}$$

$$L(E_{e^-}) = E_{e^-} \tag{2.16}$$

where $E_p$, $E_\alpha$, $E_{Be}$, $E_B$, $E_C$ and $E_{e^-}$ are energies of scattered proton, $\alpha$, $Be$, $B$, $C$ and $e^-$ respectively.

To compare simulated light output with the experimental result, light output resolution was included in simulation. The light output resolution $\triangle L$ (FWHM) of the neutron detector was parameterized [59, 68], in the terms of scintillator light output $L$ in the units of electron energy equivalent (MeVee),as

$$\triangle L = \sqrt{\alpha^2 L^2 + \beta^2 L + \gamma^2} \tag{2.17}$$

this relation describes the detector resolution due to various effects like light trans-

mission from scintillator to the photocathode($\alpha$), statistical effect of light production, attenuation, light to photon conversion($\beta$), all noise contribution($\gamma$). Hence the values of parameters $\alpha$ , $\beta$ and $\gamma$ depend on the design of the detector system as well as the condition of measurement [59]. The Values of parameters $\alpha$ , $\beta$ and $\gamma$ are obtained by matching the simulated pulse-height spectrum of $\gamma$-source $^{137}Cs$ with experiment pulse-height spectrum shown in Fig. 2.12. $^{137}Cs$ decays to metastable states of $^{137}Ba$ by emitting beta rays. Metastable states of $^{137}Ba$ decays in to ground states of $^{137}Ba$ by emitting $\gamma$-rays of energy 662 KeV. $\gamma$-ray losses energy in scintillator by inelastic scattering (Compton scattering) with electrons. Energy of the recoil electron($E_e$) depends on scattering angle($\theta$), and is given by the equation

$$E_e = \frac{{E_\gamma}^2(1 - cos\theta)}{m_0c^2 + E_\gamma(1 - cos\theta)} \tag{2.18}$$

where $E_\gamma$ is energy of incident $\gamma$-ray and $m_0c^2$ is rest mass energy of electron. Maximum amount of energy is transferred to recoil electron in head-on scattering( at angle $\theta = 180°$), and is given as

$$E_{max} = \frac{2{E_\gamma}^2}{m_0c^2 + 2E_\gamma} \tag{2.19}$$

where $E_{max}$ is called Compton edge. Light output due electron is linearly related to the energy deposition therefore unit of light output is defined in terms of electron energy. Light output produced by 1MeV electron is called 1MeVee light output.

In Fig. 2.12, experimentally measured pulse height spectrum for $^{137}Cs$ source has been compared with that calculated by means of the Monte Carlo FORTRAN code PHRESP [69] and Geant4 result. For 7" $\times$ 5" neutron detector, we obtained $\alpha = 0.15$, $\beta = 0.10$ and $\gamma = 0.02$. Pulse-height resolution function $\triangle L/L$ was taken into account by folding the calculated light output with Gaussian distribution having FWHM equal to the corresponding pulse-height resolution $\triangle L$.

The incident neutron may undergo multiple interactions in the detector depending on the neutron energy and detector dimension, leading to the production of multiple secondary charged particles. The complete trajectory of each secondary charged particle constitutes a track in GEANT4; each neutron event may usually

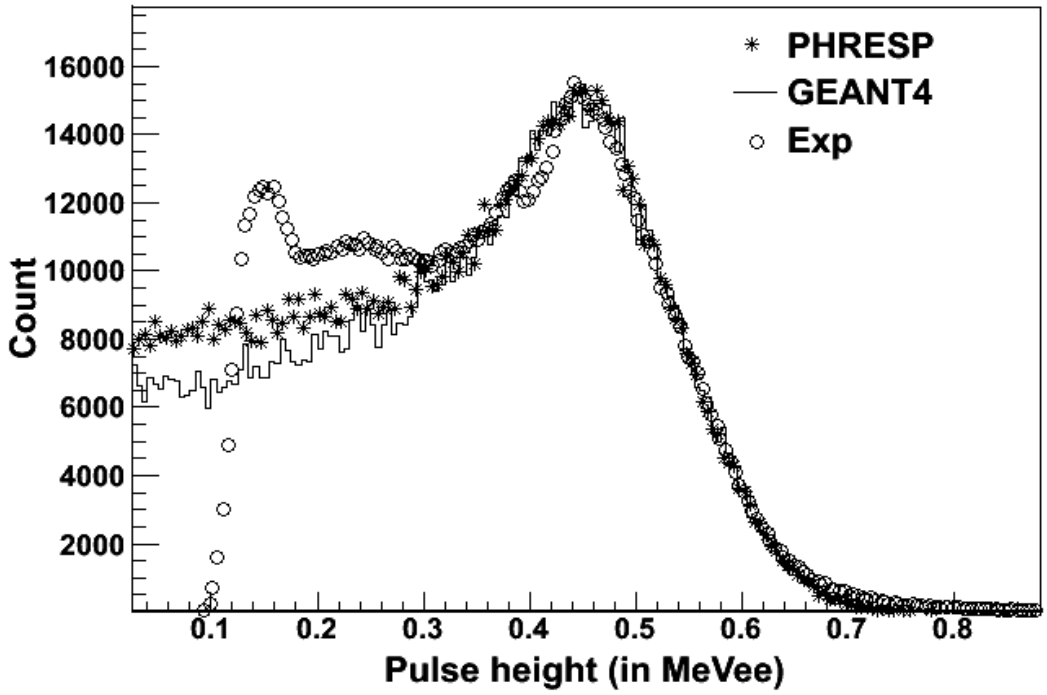


Figure 2.12: Comparison of the experimental pulse height spectrum with the GEANT4 simulated and the PHRESP [69] simulated pulse height spectra for $^{137}Cs$ source.

be made up of several tracks. Each secondary charged particle may, in its turn, undergo further interactions within the detector material, before it either looses its energy completely and is absorbed in the detector, or, deposits only a fraction of its energy in the detector and goes out of the detector. All information about the particle type, energy deposition, kinetic energy, etc., can be easily accessible in GEANT4 using tracks and steps [50]. The complete history of the tracks thus generated are then used to calculate the light output from the scintillator.

Energy deposited by secondary charged particles along their tracks is converted to light output using Cecil's prescriptions. Energy deposited by the neutron in scintillator is converted to light output by taking sum of the light output produced by all secondary charged particles to get total light output of the event.

$$L_{neutron} = \sum_{j=1}^{m} L(E_j) \tag{2.20}$$

where $E_j$ is energy deposited by secondary charged particle, m is total number of secondary charged particle produced by neutron in the detector. To include wall effect, Light output produced by each secondary particle is calculated as

$$L = L(E_K) - L(E_{KR}) \tag{2.21}$$

where $E_K$ is the kinetic energy of secondary particle produced in the scintillator material and $E_{KR}$ is it's residual kinetic energy if it escaped from the scintillator material. Thus, the energy deposited in the wall of the detector container was not converted into light output to include wall effect in GEANT4 simulation.

### 2.4.4 Discussion

Mono-energetic experimental pulse-height response of neutron of energies 2, 4, 6, 7.93, 12, 15 and 18.98 MeV are shown in Fig. 2.13, Fig. 2.14 and Fig. 2.15 along with respective the GEANT4 simulated pulse height distribution. The experimental pulse height spectra for 2, 4 and 6 MeV neutrons (Fig. 2.13) are from the present measurement, whereas the rest of the data (Fig. 2.14, 2.15, 2.16) have been taken from the literature [54]. The apparent difference of the shapes of pulse height distribution

between the present data (Fig. 2.13) and the literature data (Fig. 2.14, 2.15, 2.16) is due to the fact that the present data was taken using larger size (7" in length × 5" in diameter) detectors [70], whereas the rest of the data (Fig. 2.14, 2.15, 2.16) were obtained using small size (2" in length × 2" in diameter) detectors [54]. The difference in the pulse height resolution of the two types of detectors led to the difference in shape of the pulse height spectra in the two cases. Neutron response functions calculated with the NRESP7 code well describe the pulse height spectra of neutrons up to 20 MeV and so we also obtained response functions of mono-energetic neutron using this code to compare with GEANT4 result and experimental result.

For neutron energies below ∼10 MeV, experimental spectrum are very well reproduced by GEANT4 code with G4NDL3.14 data library. As shown in Fig. 2.16, major part of spectra is because of recoil protons produced by elastic scattering of neutron with hydrogen. It is seen that lower part of experimental result cannot be reproduced well by GEANT4 simulation for neutron energy ∼8 MeV and above. A extra peak is coming at lower part of GEANT4 simulated spectra (see Fig. 2.14 and Fig. 2.15) and the peak is gone when only proton are considered in simulation(see Fig. 2.16). That is because GEANT4 still lacks some of important reactions and NeutronHP model of Inelastic do not work well. $^{12}C(n,\alpha)^{9}Be$ gives wrong $\alpha$ events at neutron energy above ∼8 MeV. It is also reported that angular distributions of inelastically scattered neutrons from $^{12}C(n,n')^{12}C$ and alpha particles from the reaction $^{12}C(n,\alpha)^{9}Be$ are very important to include in the response programming[71], which is not properly included in GEANT4. On comparison, it is also found that NRESP7 predictions are somewhat better in representing the overall shapes of the spectra, particularly at the lower ends. These differences between NRESP7 and GEANT4 simulated results are because of the fact that NRESP7 code uses its own neutron and gamma cross-section library for physics process and different functions to calculate light output. Difference at lower part of spectra is indicative of more complete nature of the physics models used in NRESP7 which include higher order decays (like 12C(n,n′)→ 3$\alpha$ +n) which are crucial to obtain better fit at the lower

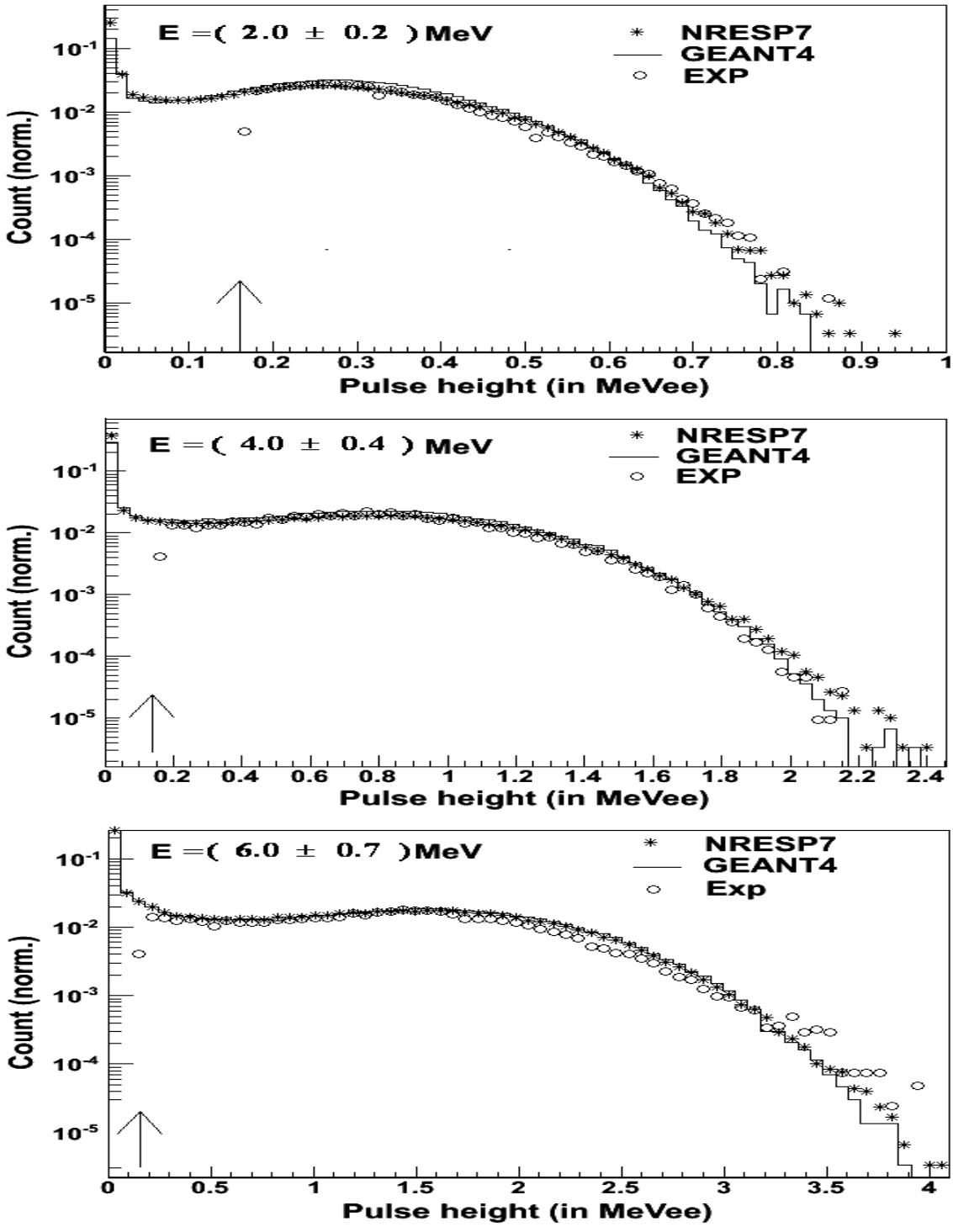


Figure 2.13: Comparison of experimental, GEANT4 simulated and NRESP7 simulated pulse height spectra for neutron energies 2, 4 and 6 MeV for source 252Cf. Detector thresholds are shown by arrows.

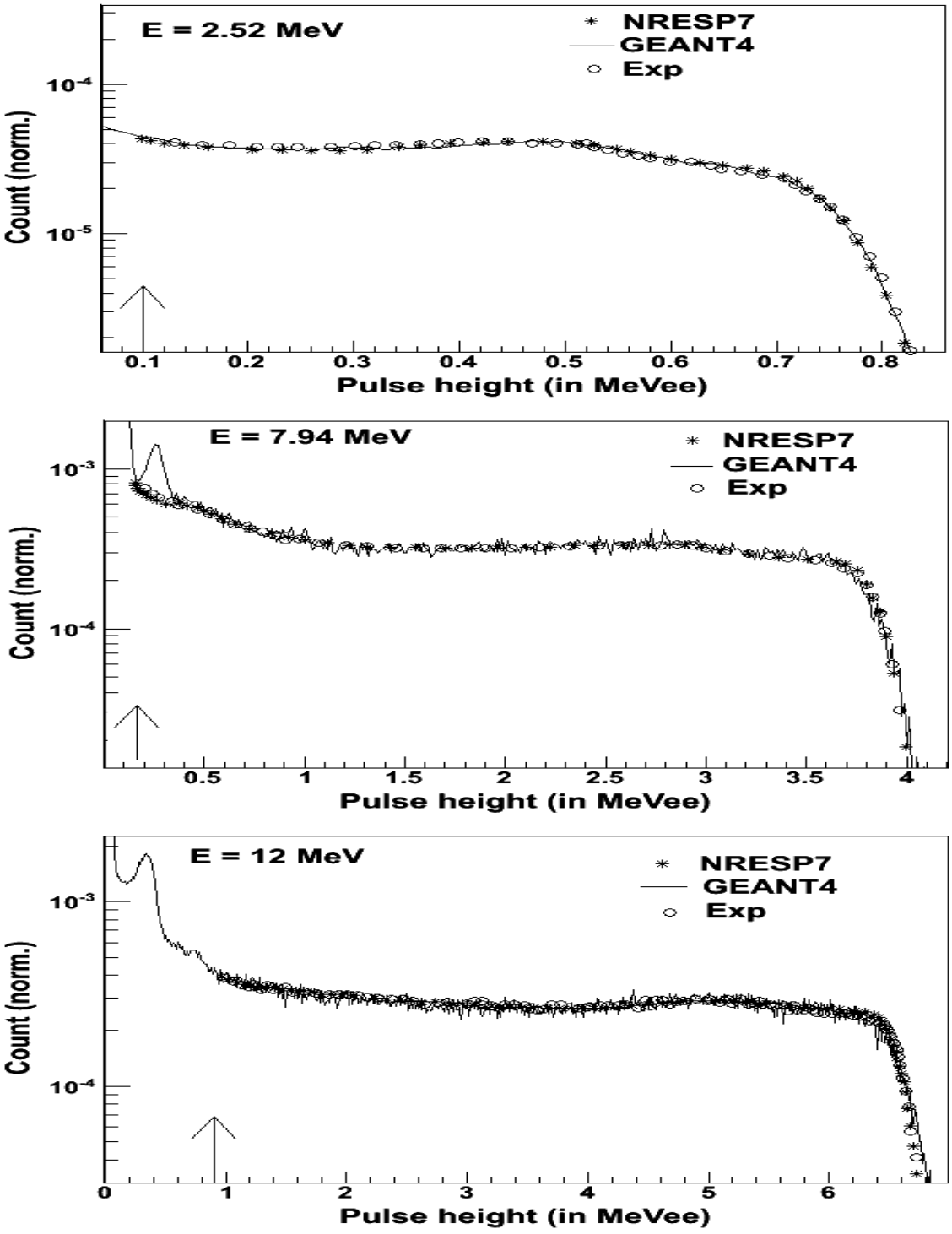


Figure 2.14: Comparison of experimental, GEANT4 simulated and NRESP7 simulated pulse height spectra for neutron energies 2.52, 7.93, and 12 MeV. Detector thresholds are shown by arrows.

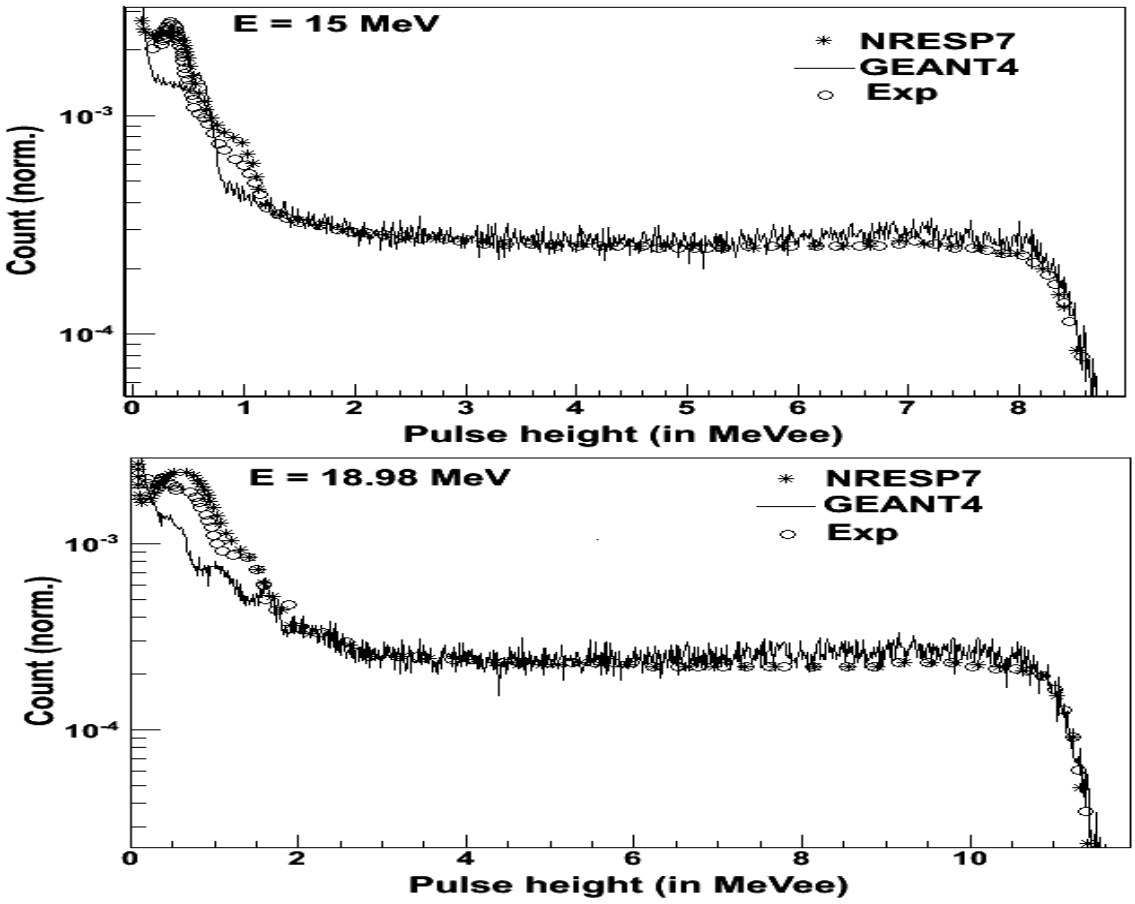


Figure 2.15: Comparison of experimental, GEANT4 simulated and NRESP7 simulated pulse height spectra for neutron energies 15 and 18.98 MeV.

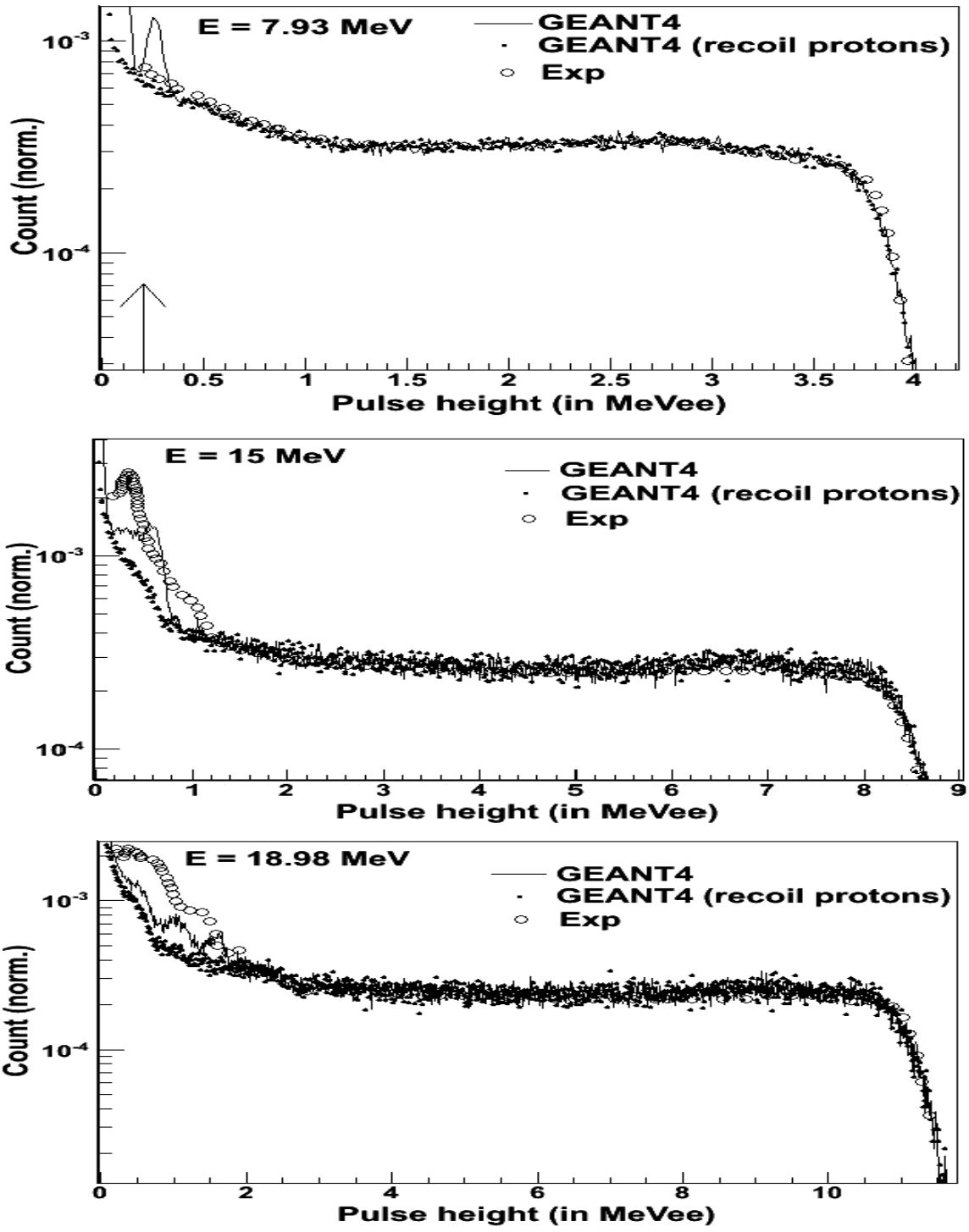


Figure 2.16: Comparison of experimental and GEANT4 simulated pulse height spectra for neutron energies 7.93, 15 and 18.98 MeV. Here line shows GEANT4 simulation considering all reaction process and dot shows recoil proton only. Detector thresholds are shown by arrows.

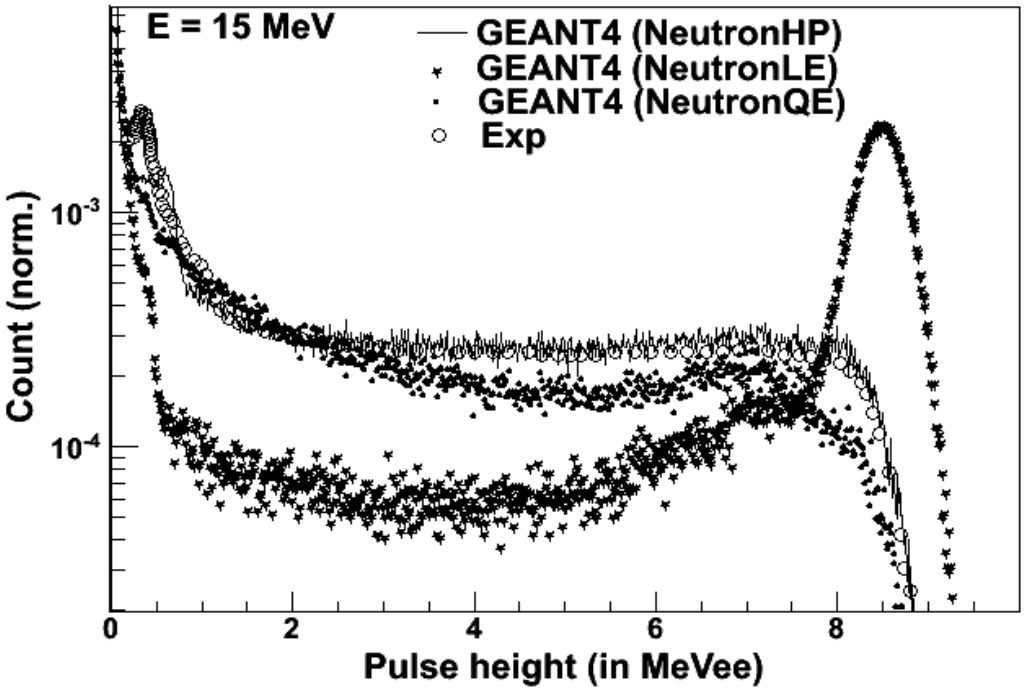


Figure 2.17: Comparison of GEANT4 simulated pulse height spectra obtained using different sets of physics model.

end of the spectra.

It is also checked that Geant4 simulation using Geisha [50] routine based data library yields results comparable to those from Geant4 with G4NDL3.14 for all energies. Geisha routine based data library is default data library for all hadronic process in Geant4 and so it is a clear that G4NDL3.14 cross-section data library works well up to it's energy range 20 MeV. We have also check the usefulness of other available models in comparison to NeutronHP models, which designed specifically for low energy neutrons up to 20 MeV. In Fig. 2.17, response function of 15 MeV neutron obtained using one sets of physics models (G4LElastic, G4LENeutronInelastic, G4LCapture and G4LFission) and other set of physics models (G4QElastic, G4LENeutronInelastic, G4LCapture and G4LFission) are shown for comparison with NeutronHP models. It was seen that NeutronHP models provide better agreement with the experimental data. The use of other cross-section data library, *i.e.*, G4HadronDataSet has also been found to make no qualitative difference.

# Chapter 3

# EXPERIMENT: STUDY OF NEUTRON EMISSION FROM COMPOUND NUCLEI $^{185}$Re*, $^{169}$Tm* and $^{201}$Tl*

## 3.1 Introduction

The aim of the present experiment is to study the variation of inverse level density parameter with angular momentum by measuring neutron evaporation from the heavy mass systems. In present work, we have chosen three systems, $^{4}$He + $^{181}$Ta , $^{4}$He + $^{165}$Ho and $^{4}$He + $^{197}$Au to populate compound nuclei $^{185}$Re$^{*}$ with the excitation energy of $\sim$ 27 - 37 MeV, $^{169}$Tm$^{*}$ with the excitation energy in the range of 26-38 MeV and $^{201}$Tl$^{*}$ with the excitation energy in the range of $\sim$ 26 - 38 MeV. Neutrons evaporated from the decay of the populated compound nuclei were measured for different $\gamma$-multiplicity ( fold ) to calculate inverse level density parameter. As seen from the table that, all three populated compound nuclei decay via $3n$ major decay channel at excitation energy $\sim$ 37 MeV and decay via $2n$ major decay channel at excitation energy $\sim$ 27 MeV. All three systems are selected with different quadrupole deformation parameter ( $\beta_2$ ) [72] to study the effect of collectivity on nuclear level density. Evaporation residues, its percentage and values of $\beta_2$ and the critical temperature $T_c$ for all three systems are shown in Table 3.1.

| System | Beam energy | Evaporation Residue | Percentage % | $\beta_2$ | $T_c$ (MeV) |
|---|---|---|---|---|---|
| $^{4}$He + $^{181}$Ta | 40 MeV | $^{182}$Re | 84.4 | 0.24 | 1.69 |
| $^{4}$He + $^{181}$Ta | 40 MeV | $^{181}$Re | 14.5 | 0.24 | 1.69 |
| $^{4}$He + $^{181}$Ta | 30 MeV | $^{183}$Re | 90.3 | 0.24 | 1.69 |
| $^{4}$He + $^{181}$Ta | 30 MeV | $^{182}$Re | 9.5 | 0.24 | 1.69 |
| $^{4}$He + $^{165}$Ho | 40 MeV | $^{166}$Tm | 88.3 | 0.28 | 2.10 |
| $^{4}$He + $^{165}$Ho | 40 MeV | $^{165}$Tm | 9.5 | 0.27 | 2.00 |
| $^{4}$He + $^{165}$Ho | 28 MeV | $^{167}$Tm | 98.3 | 0.28 | 2.10 |
| $^{4}$He + $^{165}$Ho | 28 MeV | $^{166}$Tm | 1.11 | 0.27 | 2.00 |
| $^{4}$He + $^{197}$Au | 40 MeV | $^{198}$Tl | 95.2 | -0.04 | 0.30 |
| $^{4}$He + $^{197}$Au | 40 MeV | $^{197}$Tl | 3.4 | -0.04 | 0.30 |
| $^{4}$He + $^{197}$Au | 28 MeV | $^{199}$Tl | 99.4 | -0.04 | 0.30 |
| $^{4}$He + $^{197}$Au | 28 MeV | $^{200}$Tl | 0.52 | -0.04 | 0.30 |

Table 3.1: PACE4 prediction of Evaporation residue, percentage evaporation residue produced for all systems.

## 3.2 Experimental procedure

The experiment was performed using 28 MeV and 40 MeV $^{4}$He ion beam obtained from K130 cyclotron of Variable Energy Cyclotron Centre ( VECC ), Kolkata. Self supporting foils of $^{181}$Ta of thickness 1 $mg/cm^2$, $^{165}$Ho of thickness 1 $mg/cm^2$ and $^{197}$Au of thickness 500 $\mu g/cm^2$ were used as targets to populate compound nuclei $^{185}$Re$^{*}$ from reaction $^{4}$He + $^{181}$Ta, $^{169}$Tm$^{*}$ from reaction $^{4}$He + $^{165}$Ho and $^{201}$Tl$^{*}$ from reaction $^{4}$He + $^{197}$Au, respectively . The experimental setup consisted of reaction chamber, six liquid scintillator ( BC501A ) neutron detectors of dimension $5" \times 5"$ [63], and an array of 50 $BaF_2$ $\gamma$ -ray multiplicity detectors [64]. Reaction chamber was cylindrical in shape with wall thickness $\sim$ 3mm to minimize flux loss of neutron. Each target was placed in rectangular target ladder at the center of reaction chamber. Vacuum (of the order $1.2 \times 10^{-5}$ mbar) in the reaction chamber was obtained with the help of rotary and diffusion pumps. The neutron detectors were kept at a distance of 150 cm from the center of reaction chamber at angles 25°, 32°, 45°, 105°, 120° and 152° with respect to the beam direction. The photograph of the experimental setup has been shown in Fig 3.1. Center of all neutron detectors

and center of target were kept in same horizontal plane. To achieve optimum signal shape, appropriate voltage and pulse height threshold were applied to each neutron detector ( Shown in table 3.2 ).

| Detector | Voltage (volt) -ve | Pulse height threshold (MeV) |
|---|---|---|
| detector 1 | 1455 | 0.21 |
| detector 2 | 1451 | 0.13 |
| detector 3 | 1200 | 0.17 |
| detector 4 | 1475 | 0.19 |
| detector 5 | 1280 | 0.16 |
| detector 6 | 1671 | 0.14 |

Table 3.2: Voltage and pulse height threshold applied to the detector

$BaF_2$ $\gamma$ -ray multiplicity detectors were divided into two blocks, each containing 25 detectors, and were placed on the top and at the bottom of the chamber at a distance 5 cm from the target. Two blocks of the array can be seen in Fig 3.1. Each $BaF_2$ detector was made of $BaF_2$ crystal of dimensions 3.5cm $\times$ 3.5cm $\times$ 5cm. Intrinsic time resolution of each detector is $\sim$ 450 ps and so it can be used as fast time trigger for neutron time of flight measurement. Neutrons emitted in these reactions were detected in coincidence with 50 $BaF_2$ $\gamma$ -ray multiplicity detectors to measure populated angular momentum on event by event basis. Energies of emitted neutrons were measured using TOF technique by measuring the time difference between the $BaF_2$ detector signal and the neutron detector signal and n-$\gamma$ discrimination was achieved by pulse shape discrimination (PSD) and time of flight technique. Beam dump was kept at 3 meter away from the target and shielded with the blocks of lead, concrete and paraffin to minimizes the background neutrons and $\gamma$-rays coming from beam dump. Blank frame run was carried out to estimate background neutrons from the neutrons coming from the target.

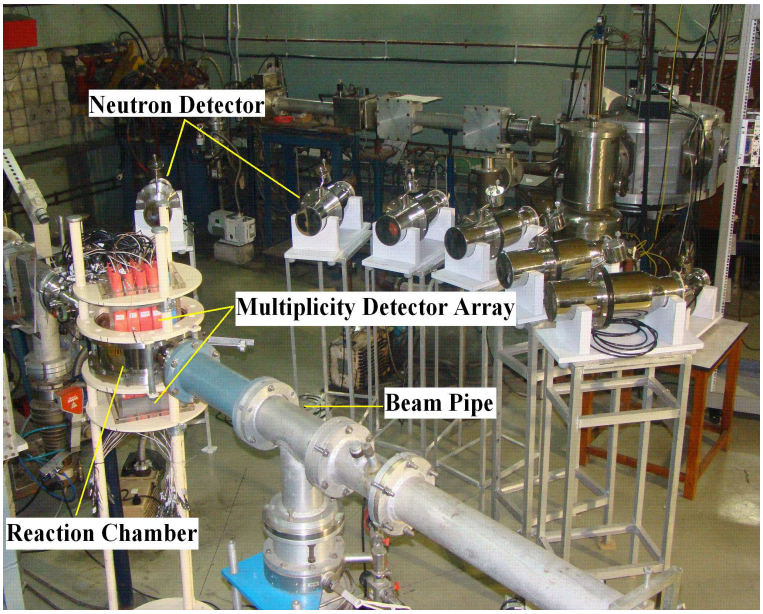


Figure 3.1: Picture of Experimental setup

### 3.2.1 Electronics Setup

The block diagram of the electronics setup used in all these experiments is shown in Fig. 3.2. First, analog signals of all the neutron detectors were fed to splitters to split each signal into two signals without any loss in amplitude due to cables. Splitter is a passive device which generates multiple output signal from single input with specific phase and amplitude characteristics to match the impedance of devices. One output signal from each splitter was connected to one input channel of Mesytec MPD4 module to obtain pulse height(PH), zero cross over (ZCO) and logic pulse CFD of neutron detector. Mesytec MPD4 is a four channel particle discriminator module used to separate neutron signals from $\gamma$ signals using pulse shape discrimination technique(PSD). PSD technique has been discussed in detail in previous Chapter. Two outputs of the MPD4, pulse height(PH) and zero cross over(ZCO), were connected to analog to digital converter VME ADC (CAEN V792) to convert and store the data in digital forms. Third output signal of MPD4, logic pulse CFD, was connected to Gate and Delay Generator(GDG) to adjust cable delay in neutron

signals. Delayed CFD pulse was used as stop input of Time to Digital Conversion (TDC) to obtain neutron time of flight information.

Other output of the splitter was connected to leading edge discriminator (LED) to generate logic OR of the all six neutron detectors. Analog signals of top and bottom $BaF_2$ $\gamma$ -ray multiplicity detectors were fed to 16 channel CAMAC constant fraction discriminators (CFD, CAEN C808) to obtain logic OR of top and bottom arrays. The output currents ( 1 mA per hit ) of the CFDs were summed using Linear-Fan-in module (CAEN N401). Summed output current was fed to VME QDC (CAEN V792) and integrated for a gate duration 30ns to extract the experimental fold distribution by applying condition Fold $F \geq 2$. Fold $F$ was taken as the number of $BaF_2$ detectors fired simultaneously in a single event. A trigger pulse is obtained from $BaF_2$ array when one of the detectors from top array fired in coincidence with one of the detectors from bottom array, above 200 KeV threshold. Master trigger for all ADC, QDC and TDC was generated when one of the neutron detector fired in coincidence with at least two $BaF_2$ detectors fired . This was done by taking logic AND between logic OR of top and logic OR of bottom $BaF_2$ arrays signals. Finally on-line data acquisition was done on event by event basis using VME data acquisition system ( VME DAQ ) developed at VECC( Fig 3.2).

## 3.3 Data analysis

Off-line data analysis was done using ROOT based data analysis software developed by scientists of VECC using LINUX environment. The programme allows to access data of neutron detectors (pulse height, zero cross over, time of flight of neutron) along with $BaF_2$ detectors ($\gamma$ fold) on event by event mode. Thus, experimental neutron energy spectrum for different $\gamma$ folds was extracted to compared with theoretical result.

### 3.3.1 Extraction of angular momentum distribution

Fold distributions of yrast $\gamma$ rays were measured using 50 $BaF_2$ $\gamma$ - ray multiplicity detectors in coincidence with neutron detectors (see Fig 3.3). Experimental fold distributions were reproduced using GEANT3 [73] simulation by including real experimental conditions like detector threshold and trigger conditions in simulation. Two blocks of 25 $BaF_2$ $\gamma$ -ray multiplicity detectors were constructed and placed on the top and at the bottom of the chamber at a distance 5 cm from the target in the GEANT3 simulation [73]. 200,000 events were thrown on $BaF_2$ $\gamma$ - ray multiplicity detectors to reproduce GEANT4 simulation of fold distribution. The incident energy distribution of $\gamma$ - rays was taken as a Gaussian with peak at 0.5 MeV and full with half maximum (FWHM) at 0.65 MeV. Incident angular momentum distributions of all nuclear reactions were calculated using the statistical model code CASCADE [74]. Incident multiplicity distribution was obtained by transforming calculated angular momentum distribution (J ) into multiplicity distribution ( M ) using relation

$$J = 2M + C \tag{3.1}$$

where $C$ is the parameter which takes care of $\gamma$ rays other than yrast $\gamma$ rays. Factor 2 is because yrast $\gamma$ rays are emitted due to mainly E2 transitions. Parameter $C$ is estimated by comparing experimental fold distribution with GEANT3 simulated fold distribution. Multiplicity distribution is actual distribution emitted from compound nucleus where as fold distribution is a measured distribution.

In GEANT3 simulation, obtained incident multiplicity distribution P(M) was triangular in shape and can be given as

$$P(M) = \frac{2M + 1}{1 + exp(\frac{M - M_{max}}{\delta M})} \tag{3.2}$$

where, $M$, $M_{max}$ and $\delta M$ are multiplicity ( actual number of $\gamma$ - rays emitted in a event ), maximum of this distribution and the diffuseness factor, respectively. Angular momentum distributions for different folds for system $^{4}$He + $^{181}$Ta at beam

energy 40 MeV is shown in Fig 3.4. Average angular momentum values for all the systems are given in table 3.3

| System | Beam energy (MeV) | Fold | $< J > (\hbar)$ |
|---|---|---|---|
| $^{4}$He + $^{181}$Ta | 30 | 2 | $12 \pm 4$ |
| $^{4}$He + $^{181}$Ta | 30 | 3 | $14 \pm 4$ |
| $^{4}$He + $^{181}$Ta | 30 | $\geq$4 | $17 \pm 5$ |
| $^{4}$He + $^{181}$Ta | 40 | 2 | $13 \pm 4$ |
| $^{4}$He + $^{181}$Ta | 40 | 3 | $15 \pm 4$ |
| $^{4}$He + $^{181}$Ta | 40 | $\geq$4 | $18 \pm 5$ |
| $^{4}$He + $^{165}$Ho | 28 | 2 | $12 \pm 5$ |
| $^{4}$He + $^{165}$Ho | 28 | 3 | $15 \pm 5$ |
| $^{4}$He + $^{165}$Ho | 28 | $\geq$4 | $18 \pm 6$ |
| $^{4}$He + $^{165}$Ho | 40 | 2 | $15 \pm 5$ |
| $^{4}$He + $^{165}$Ho | 40 | 3 | $18 \pm 5$ |
| $^{4}$He + $^{165}$Ho | 40 | $\geq$4 | $21 \pm 6$ |
| $^{4}$He + $^{197}$Au | 40 | 2 | $15 \pm 5$ |
| $^{4}$He + $^{197}$Au | 40 | 3 | $18 \pm 4$ |
| $^{4}$He + $^{197}$Au | 40 | $\geq$4 | $21 \pm 5$ |

Table 3.3: Average angular momentum values for all the systems.

### 3.3.2 Experimental neutron energy spectra for different fold

Neutron energy spectrum for different folds was calculated using Time Of Flight method by putting cut on corresponding $\gamma$ fold as shown in Fig 3.3. Neutron was separated from $\gamma$ events using pulse shape discrimination technique. Pure neutron TOF spectrum was extracted by putting proper two dimensional gate over neutron events in zero cross over vs time of flight spectrum as shown in Fig. 3.5. $\gamma$-peak of TOF spectrum was used as reference time to calibrate TDC to convert neutron TOF spectrum into neutron energy spectrum. This is because $\gamma$ emitted from the compound nucleus always takes same time to reach neutron detector due to it's constant light speed. Logic pulses of different time widths were applied to TDC using standard time calibrator to convert TOF spectrum in time from channel number

(see Table 3.4). Plot of pulse width(t) vs channel no(ch) is a straight line with slope m and intercept c

| Pulse width (ns) | Channel number |
|---|---|
| 20 | 308 |
| 40 | 697 |
| 60 | 1094 |
| 80 | 1483 |
| 100 | 1873 |
| 120 | 2256 |
| 140 | 2659 |
| 160 | 3049 |
| 180 | 3446 |

Table 3.4: Applied pulses and channel no of TDC used for detector 1.

$$t = m(ch) + c \tag{3.3}$$

Flight time ($t_n$) taken by neutron to reach a neutron detector from compound nucleus, was calculated from neutron TDC channel no ($ch_n$) as

$$t_n = m(ch_n - ch_\gamma) + c + t_\gamma \tag{3.4}$$

where ($t_\gamma$) and ($ch_\gamma$) are flight time and TDC channel no of $\gamma$ ray, respectively. Neutron energy spectrum was generated by calculating neutron energy using non relativistic equation of kinetic energy

$$E_n = \frac{1}{2} m_n v^2 = \frac{1}{2} m_n \left( \frac{l}{t_n} \right)^2 \tag{3.5}$$

where, $m_n$ is the mass of neutron, l is the flight path ( 150cm ) and $t_n$ is neutron time of flight. The prompt $\gamma$ peak has been taken as time reference. The measured TOF spectrum were converted into energy spectrum by using proper jacobian. The transformation from the time domain to the energy domain has been done by knowing the fact that the events (counts) must be conserved, i.e. the number of events,

$N(t_n)$, in a time bin, $\delta t_n$, for a time domain spectrum must be equal to the number of events, $N(E_n)$, in the corresponding energy bin, $\delta E_n$, for the energy domain spectrum. So the transformation can be done as

$$N(E_n)\delta E_n = N(t_n)\delta t_n \tag{3.6}$$

Using equation of kinetic energy, one can drive the jacobian for time to energy conversion

$$\left| \frac{\delta t_n}{\delta E_n} \right| = \frac{t_n}{2E_n} \tag{3.7}$$

Hence,

$$N(E_n) = N(t_n)\frac{t_n}{2E_n} \tag{3.8}$$

Using above Eq 3.8, counts in each bin of time spectrum was converted to counts in corresponding bin of energy spectrum. The energy spectrum that obtained, was corrected by folding neutron detector efficiency. Efficiency of neutron detector of dimension $5" \times 5"$ was estimated using Monte Carlo computer code NEFF [59].

To compare with theoretical result, which is in center of mass frame, experimental neutron energy spectrum was transformed to center of mass(cm) frame from laboratory(lab) frame. Velocity of the compound nucleus in lab frame ($\vec{V}_{cnL}$) is calculated using momentum conservation principal in lab frame as

$$\vec{V}_{cnL} = \frac{m_p}{m_p + m_T}\vec{V}_{pL} \tag{3.9}$$

where $m_p$, $m_T$ and $\vec{V}_{pL}$ are mass of projectile nucleus, mass of target nucleus and velocity of projectile in lab frame, respectively. Velocity of neutron in center of mass frame is written as (see Fig 3.6 )

$$\vec{V}_{nCM} = \vec{V}_{nL} - \vec{V}_{cnL} \tag{3.10}$$

so magnitude of $\vec{V}_{nCM}$ is

$$V_{nCM} = \sqrt{V_{nL}^2 + V_{cnL}^2 - 2V_{nL}V_{cnL}cos\theta_L} \tag{3.11}$$

where $\theta_L$ is angle of emitted neutron with respect to the direction of incident projectile in lab frame.

Now, neutron energy in center of mass was calculated using equation $E_{nCM} = \frac{1}{2} m_n V_{nCM}^2$. From neutron scattering kinematics, Lorentz invariant double differential cross section can be transfer from lab to cm frame as

$$\left(\frac{d^2\sigma}{dE_{nCM}d\Omega}\right)_{CM} = \left(\frac{d^2\sigma}{dE_n d\Omega}\right)_L \frac{V_{nCM}}{V_{nL}} \tag{3.12}$$

where $\left(\frac{d^2\sigma}{dE_{nCM}d\Omega}\right)_{CM}$ and $\left(\frac{d^2\sigma}{dE_n d\Omega}\right)_L$ are double differential cross sections of neutron emission from compound nucleus in center of mass frame and lab frame, respectively. The obtained experimental energy spectra in center of mass frame for different folds were shown in Fig 3.7-3.11.

### 3.3.3 Theoretical neutron energy spectra

Theoretical neutron energy spectrum was calculated using statistical model based computer code CASCADE [74]. GEANT3 [64, 73] simulated angular momentum fold distribution was given as input of the CASCADE code to extract theoretical spectrum for different folds. In the calculation, it is assumed that compound nucleus is formed in statistical equilibrium with respect to all degree of freedom. Its spin distribution is derived from fusion cross section using strong absorption model. Particle evaporation of compound nucleus is calculated using Hauser-Feshbach formula. Only neutron, proton, alpha and $\gamma$-ray emission is considered in the calculation. A statistical model calculation can be described in three steps:

1. **Calculation of fusion cross section of compound nucleus**

   The fusion cross section of formation of compound nucleus was calculated using eq 1.30. Transmission coefficient depends on energy and orbital angular momentum and it is estimated using Fermi distribution given by eq 1.32. Here value of diffuseness constant $d$ is estimated using Optical model potential.

2. **Calculation of Statistical decay probability of particles from equilibrated system**

The formula for particle emitting probability was obtained from the reciprocity theorem using transmission coefficients. The rate for emitting a particle from compound nucleus to form a product nucleus was calculated using eq 1.34. Here transmission coefficients were obtained using optical model.

3. **Calculation of level density**

It is clear from the eq 1.34 that calculation of level density is necessary to calculate particle emission probability. Estimation of level density and its relation with excitation energy and angular momentum is required in statistical model calculation. For simple system with $A$ particles with an excitation energy $E^*$, most general expression of level density is given by eq 1.36. This equation was approximated using the Fermi-gas model for a spherical nucleus as given in eq 1.37. Values of the all parameters used in eq 1.37 are given in table 3.5.

| Parameter | Value |
|---|---|
| $\delta_1$ | $0.9 \times 10^{-5}$ |
| $\delta_2$ | $0.2 \times 10^{-8}$ |
| $\Delta_P$ | $12/\sqrt{A}$ |
| $\Im_0$ | $\frac{2}{5}A^{5/3}{r_0}^2$ |
| $r_0$ | 1.17 |

Table 3.5: Values of parameters used in Eq 1.37.

For ground state deformed nuclei, at low excitation energy, collective motion give rise to rotational and vibrational bands enhancing the level density above the single - particle value. This enhancement was included by using collective enhancement factor as shown in eq 1.50. Enhancement factor due to rotational bands is necessary in deformed nuclei while enhancement factor due to vibrational bands is necessary in spherical nuclei.

The level density parameter ( $a$ ) from the single particle levels near the Fermi surface depends on the shell structure and the shape of the nucleus, which in turn depend on the excitation energy. To include shell effect into statistical calculation, we used an energy-dependent level density parameter introduced by Ignatyuk *et.al*, [17]. This expression was given by eq 1.47 and discussed in Chapter.1.

Calculated energy spectra were convoluted by time of flight energy resolution of neutron detector by multiplying theoretical double differential cross section $\left(\frac{d^2\sigma}{dE_n d\Omega}\right)_{CM}$ with response matrix $R_{i,j}$. Two dimensional response matrix $R_{i,j}$ was calculated using Gaussian distribution function with width equal to time of flight resolution

$$R_{i,j}(E^i{}_n) = \frac{1}{\sqrt{2\pi}\sigma_i} exp\left(-\frac{1}{2}\left(\frac{E^i{}_n - E^j{}_n}{\sigma_i}\right)^2\right) \tag{3.13}$$

where variance $\sigma_i$ of Gaussian function is related to full width at half maximum ($FWHM_i$) as

$$\sigma_i = \frac{FWHM_i}{2.35} \tag{3.14}$$

where $FWHM_i$ is obtained by calculating the time of flight energy resolution of neutron detector using eq 2.10. Now, convolution was done using equation

$$\begin{pmatrix} \left(\frac{d^2\sigma}{dE_n d\Omega}\right)^1{}_{CM} \\ \left(\frac{d^2\sigma}{dE_n d\Omega}\right)^2{}_{CM} \\ ..... \\ \left(\frac{d^2\sigma}{dE_n d\Omega}\right)^i{}_{CM} \end{pmatrix} = \begin{pmatrix} \left(\frac{d^2\sigma}{dE_n d\Omega}\right)^1{}_{CM} \\ \left(\frac{d^2\sigma}{dE_n d\Omega}\right)^2{}_{CM} \\ ..... \\ \left(\frac{d^2\sigma}{dE_n d\Omega}\right)^j{}_{CM} \end{pmatrix} \begin{pmatrix} R_{1,j} & R_{1,j} & .... & R_{1,j} \\ R_{2,j} & R_{2,j} & .... & R_{2,j} \\ ..... & ..... & .... & .... \\ R_{i,j} & R_{i,j} & .... & R_{i,j} \end{pmatrix} \tag{3.15}$$

where $\left(\frac{d^2\sigma}{dE_n d\Omega}\right)^j{}_{CM}$ are convoluted double differential cross section in center of mass frame. Thus, obtained theoretical neutron energy spectra of different folds for all three systems are shown in Fig 3.7, 3.8, 3.9, 3.10 and 3.11, respectively.

### 3.3.4 Results and Discussions

In this work, we have measured $\gamma$-ray fold gated neutron energy spectra in the reactions that populates compound nucleus in the mass region $A \sim 169 - 201$ at excitation energy of range $\sim$ 26-38 MeV. Theoretical energy spectra for different $\gamma$ folds were fitted to corresponding experimental energy spectra using $\chi^2$ minimization technique. Most probable values of $k$ and corresponding value of $\chi^2$ for least square fitting was achieved by varying inverse level density parameter ($k$) in calculations. $\chi^2$ was taken as

$$\chi^2 = \sum_{i}^{N} \frac{[y_i - f(k,i)]^2}{{\sigma_i}^2} \tag{3.16}$$

where $y_i$ and $f(k,i)$ are measured and calculated double differential cross section of $i^{th}$ energy bin for inverse level density parameter $k$. $\sigma_i$ is statistical error in experimentally measured cross section of $i^{th}$ energy bin. According to definition, best fit $k$ value occurs when $\chi^2$ is minimum.

The experimental neutron energy spectra for different $\gamma$ -ray folds at angle 152° along with corresponding CASCADE prediction for all system are shown in Fig 3.7, Fig 3.8, Fig 3.9, Fig 3.10, and Fig 3.11. Obtained best fit values of inverse level density parameters ($k$) are tabulated in table 3.6. It is seen that the value of level density parameter $k$ remain almost constant with increase in $\gamma$-ray folds for all system. Thus, dependence of the angular momentum $J$ on nuclear level density is almost negligible in all five reactions ( see table 3.6 ). Dependence of angular momentum on level density is taken care through the rotational energy $E_{rot}$ by introducing effective moment of inertia $\Im_{eff}$. $\Im_{eff}$ is parameterized by deformability parameters ($\delta_1$ and $\delta_2$), which are adjusted to include effect of angular momentum dependent deformation. In present case, it is observed that variation of deformability parameters $\delta_1$ and $\delta_2$ do not effect the shape of the energy spectra and therefore the effect of $\delta_1$ and $\delta_2$ on level density is insignificant [75].

Average temperature (T) of compound nuclei produced in both the above systems are above their corresponding critical temperature ($T_c$) and therefore collective

| System | Beam energy | Fold | k (MeV) | Temperature (MeV) |
|---|---|---|---|---|
| $^{4}$He + $^{181}$Ta | 30 MeV | All | 9.7 ± 0.6 | 1.18 |
| | ” | 2 | 9.8 ± 0.5 | 1.19 |
| | ” | 3 | 9.9 ± 0.8 | 1.18 |
| | ” | ≥4 | 10.2 ± 0.9 | 1.17 |
| $^{4}$He + $^{181}$Ta | 40 MeV | All | 10.9 ± 0.5 | 1.44 |
| | ” | 2 | 11.1 ± 0.3 | 1.46 |
| | ” | 3 | 10.9 ± 0.5 | 1.44 |
| | ” | ≥4 | 10.8 ± 0.6 | 1.42 |
| $^{4}$He + $^{165}$Ho | 28 MeV | All | 7.9 ± 0.5 | 1.06 |
| | ” | 2 | 8.0 ± 0.5 | 1.08 |
| | ” | 3 | 7.7 ± 0.6 | 1.05 |
| | ” | ≥4 | 7.8 ± 0.6 | 1.04 |
| $^{4}$He + $^{165}$Ho | 40 MeV | All | 9.3 ± 0.5 | 1.37 |
| | ” | 2 | 9.5 ± 0.4 | 1.42 |
| | ” | 3 | 9.2 ± 0.4 | 1.38 |
| | ” | ≥4 | 9.2 ± 0.6 | 1.36 |
| $^{4}$He + $^{197}$Au | 40 MeV | All | 9.2 ± 0.5 | 1.26 |
| | ” | 2 | 9.1 ± 0.4 | 1.28 |
| | ” | 3 | 9.1 ± 0.5 | 1.27 |
| | ” | ≥4 | 9.0 ± 0.5 | 1.25 |

Table 3.6: Best fitted inverse level density parameter and temperature for all systems.

enhancement in level density due to ground state deformation is expected to more significant. To study the temperature ( or excitation energy ) dependence of nuclear level density , average temperature of populated compound nuclei was estimated using formula $U = aT^2$. Excitation energy ( $U$ ) of residual nucleus is given by

$$U = E^* - E_{rot} \tag{3.17}$$

where $E^*$ and $E_{rot}$ are initial excitation energy and rotational energy. Initial excitation energies were calculated using FORTRAN code PACE4. Rotational energies of compound nucleus were calculated using eq 1.38. For systems used in present work, approximated range of $E^*$ and $E_{rot}$ were $\sim 26 - 38$ MeV and $\sim 0.8 - 2.5$ MeV, respectively. As seen from the table 3.6, for All fold, values of inverse level density parameter ($k$) increases from $9.7 \pm 0.6$ to $10.9 \pm 0.5$ as the average temperature ($T$) ( or excitation energy ) of compound nuclei increases from 1.18 MeV to 1.44 MeV for systems $^{4}$He + $^{181}$Ta . Similarly, values of inverse level density parameter ($k$) increases from $7.9 \pm 0.5$ to $9.3 \pm 0.5$ as the average temperature ($T$) ( or excitation energy ) of compound nuclei increases from 1.06 MeV to 1.37 MeV for systems $^{4}$He + $^{165}$Ho. Above observation suggest that there has been a relative decrement in nuclear level density at higher temperature for both systems. This decrement in nuclear level density is directly related to nuclear deformation due to shell effects. The deformation due to the shell effect decrease as temperature increase and therefore relative enhancement in level density is reduced at higher temperature for both systems.

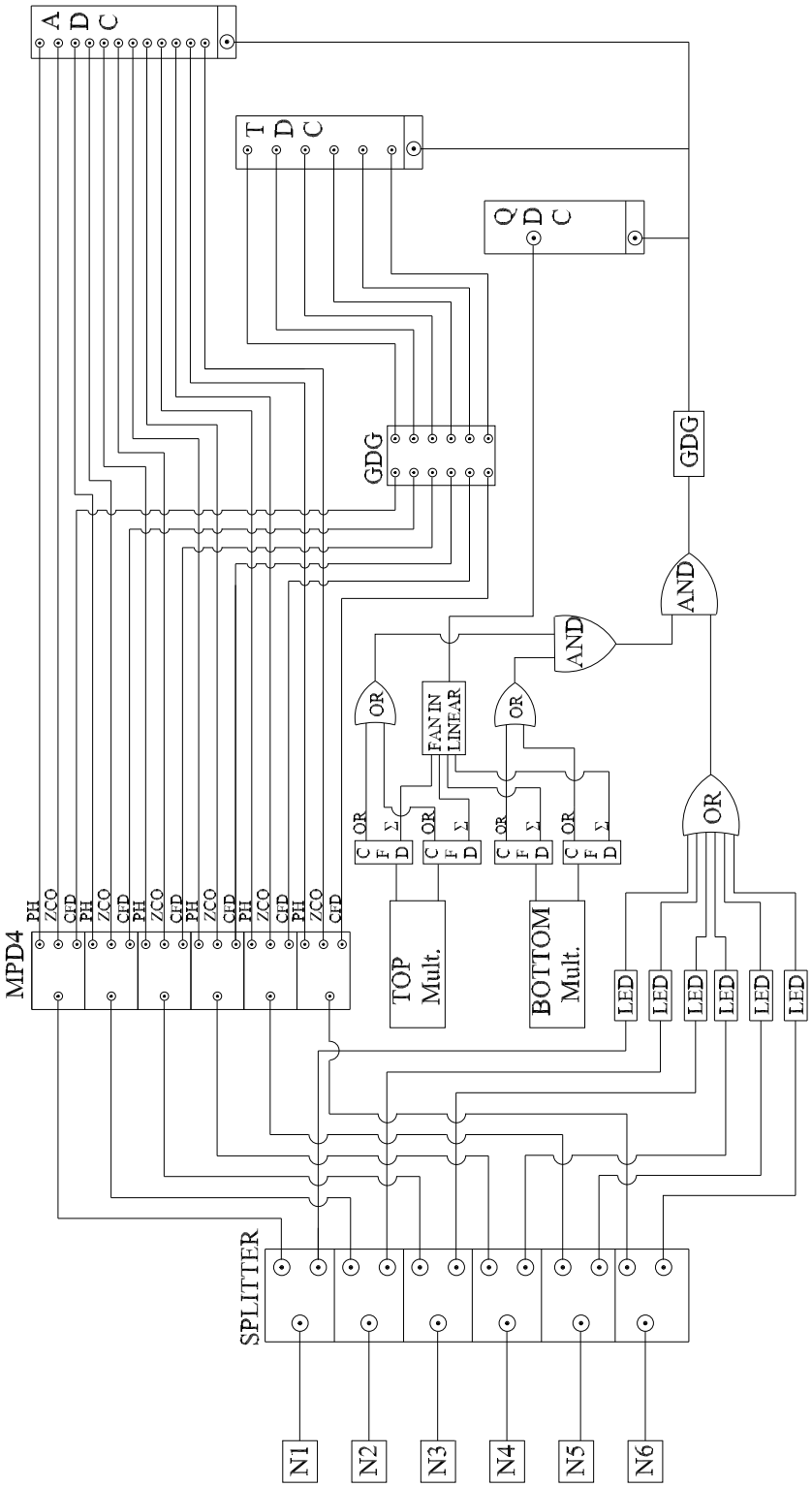


Figure 3.2: Block diagram of electronic setup used in beam experiment.

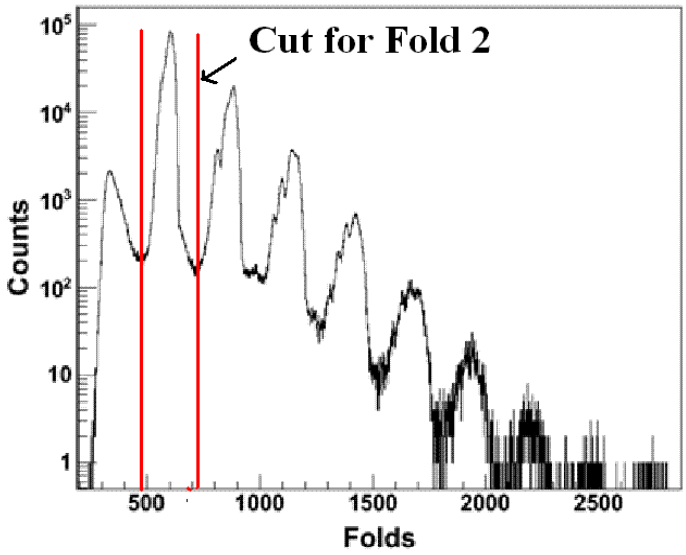


Figure 3.3: Experimental fold distribution with the cut over fold 2.

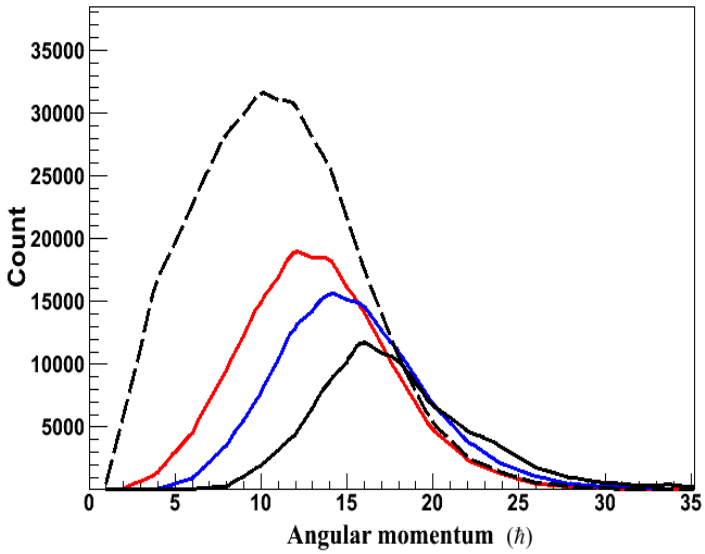


Figure 3.4: Incident angular momentum distribution used in GEANT3 ( for system $^{4}$He + $^{181}$Ta at beam energy 40 MeV ) are shown using dashed line in the figure. Angular momentum distributions obtained for fold 2, fold 3 and fold 4 & more are shown by solid red, solid blue and solid black line, respectively.

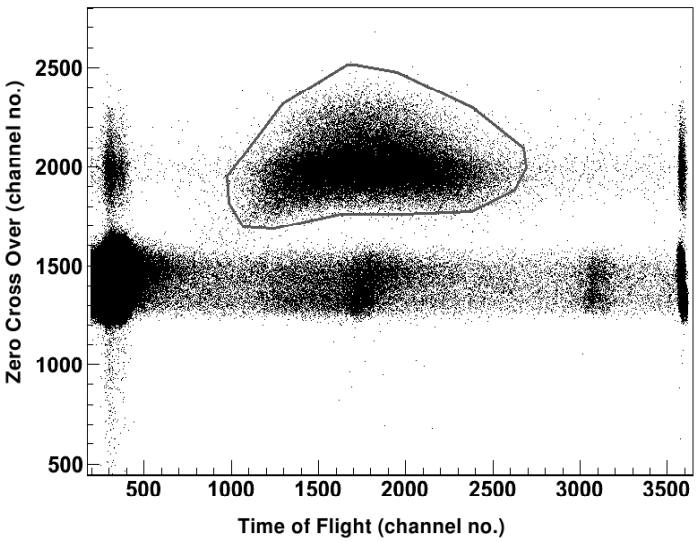


Figure 3.5: Zero cross over vs time of flight spectrum.

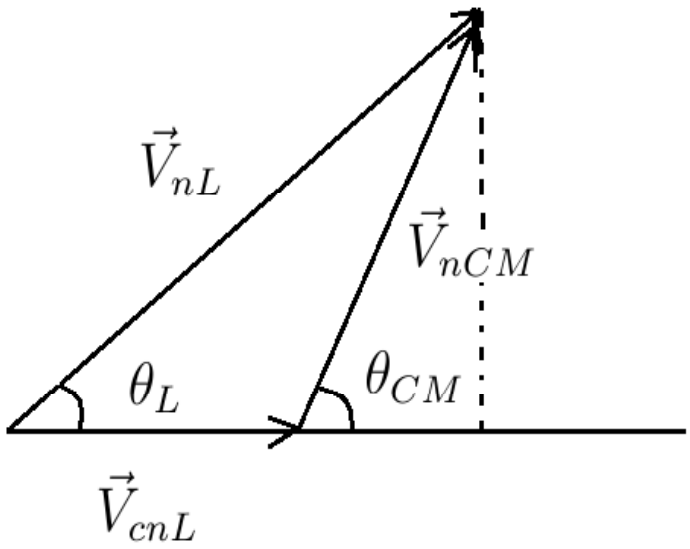


Figure 3.6: Figure shows the relation between velocities of evaporated neutron in laboratory frame and center of mass frame.

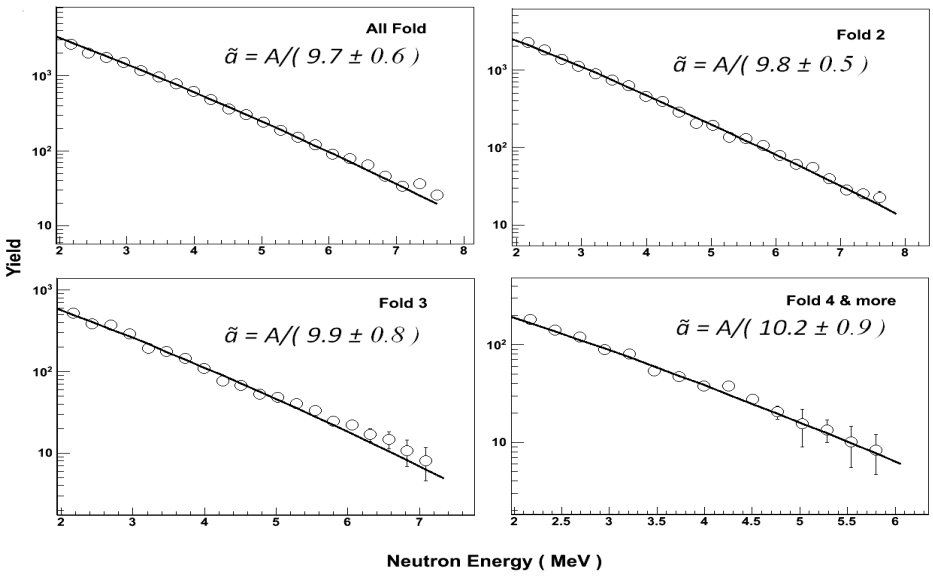


Figure 3.7: Experimental fold gated neutron spectra ( circle ) along with the theoretical result (continuous lines) calculated using statistical model code CASCADE for $^{4}$He + $^{181}$Ta at $E_{lab}$ = 30 MeV.

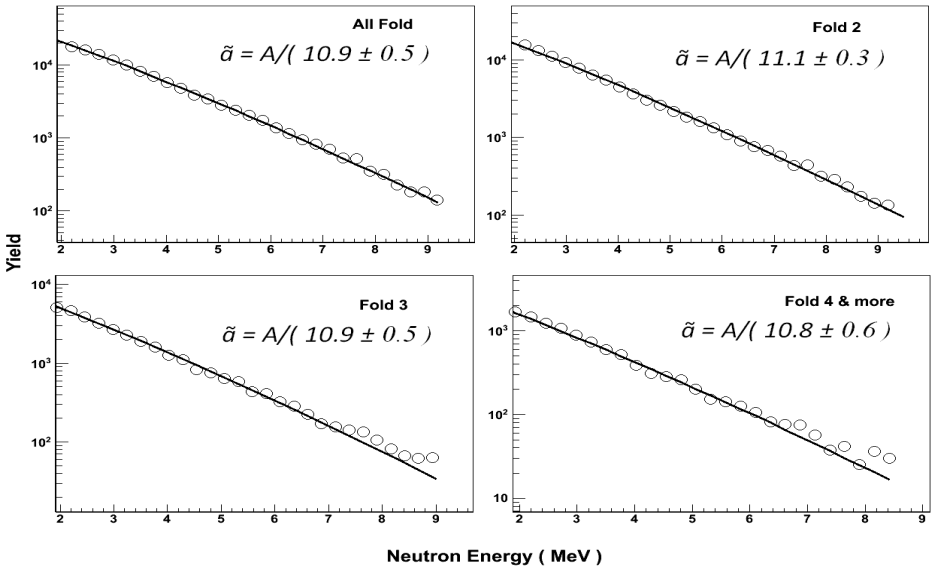


Figure 3.8: Experimental fold gated neutron spectra ( circle ) along with the theoretical result (continuous lines) calculated using statistical model code CASCADE for $^{4}$He + $^{181}$Ta at $E_{lab}$ = 40 MeV.

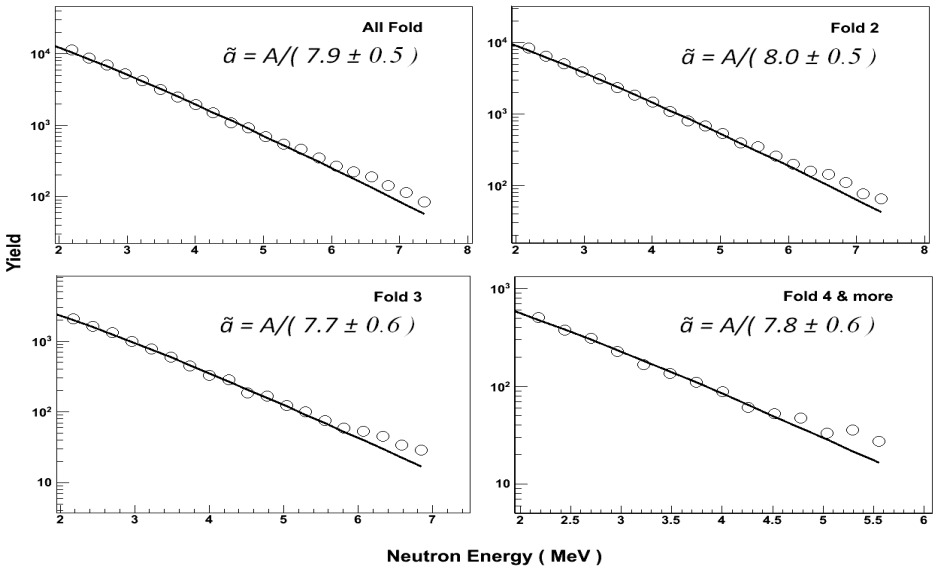


Figure 3.9: Experimental fold gated neutron spectra ( circle ) along with the theoretical result (continuous lines) calculated using statistical model code CASCADE for $^{4}$He + $^{165}$Ho at $E_{lab}$ = 28 MeV.

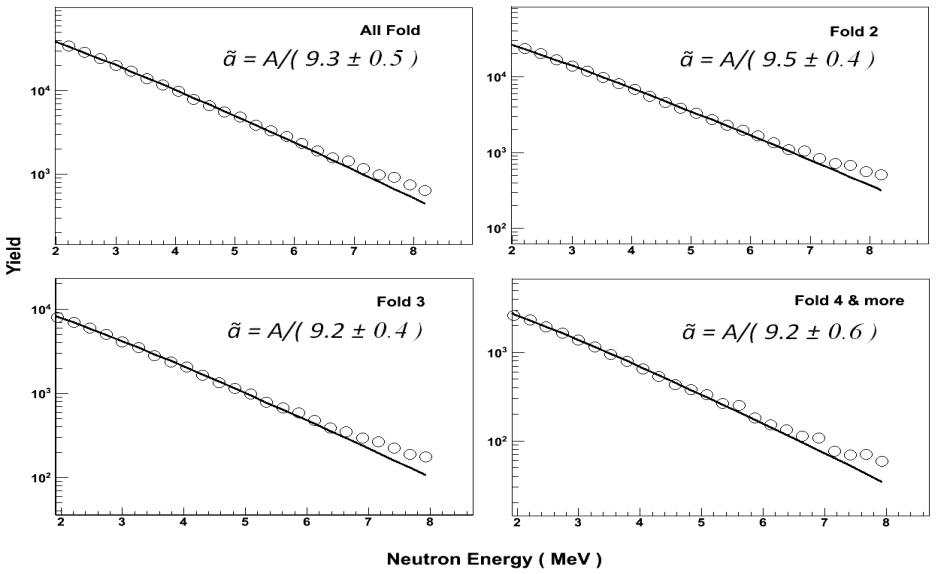


Figure 3.10: Experimental fold gated neutron spectra ( circle ) along with the theoretical result (continuous lines) calculated using statistical model code CASCADE for $^{4}$He + $^{165}$Ho at $E_{lab}$ = 40 MeV.

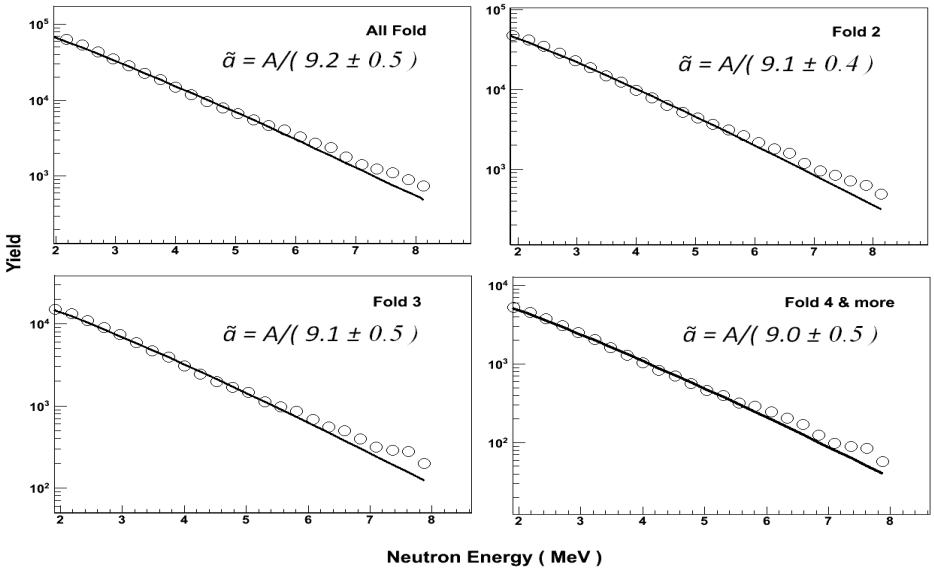


Figure 3.11: (Experimental fold gated neutron spectra ( circle ) along with the theoretical result (continuous lines) calculated using statistical model code CASCADE for $^{4}$He + $^{197}$Au at $E_{lab}$ = 40 MeV.

# Chapter 4

# SUMMARY AND CONCLUSION

The aim of the present work was to study the angular momentum dependence of nuclear level density of heavy nuclei by measuring the energy distribution of neutrons evaporated from them. Organic liquid scintillator (BC501A) based neutron detectors were developed under the present theses work. Energy of evaporated neutrons are measured using time of flight technique using neutron detector and $BaF_2$ multiplicity detector. Neutron detectors of various dimensions were fabricated to study various characteristics of detectors ( pulse height response, detection efficiency , neutron-$\gamma$ ray discrimination ). To measure the quality of pulse shape discrimination, Figure of merit of scintillator detectors of size 5" diameter $\times$ 5" length and 5" diameter $\times$ 7" length was experimentally measured using $^{241}AmBe$ source. It was seen that neutron and $\gamma$ events are very well separated in both the detectors. It was also found that the value of M decreases with increase in the detector length due to higher reduction in light collection by PMT ( since dimensions of PMT were same in both the detector ) and higher time spread in arrival of light at PMT. Response function of mono-energetic neutrons from continuous neutron energy field have been studied comprehensively up to 20 MeV. Experimental response functions for neutron have been obtained from present measurement as well as from the literature [54]. The experimental pulse height response was calibrated using the Compton edges of two mono-energetic $\gamma$-sources ($^{22}Na$ and $^{137}Cs$). Mono-energetic neutron response functions have been simulated using GEANT4 toolkit version 4.9.2 using neutron cross-section data library G4NDL3.14. In GEANT4 simulation, wall effect was prop-

erly included by placing a container around BC501A liquid in detector construction of simulation. NeutronHP physics models were used to incorporate elastic, inelastic, capture and fission process of neutron with scintillation material in simulation. In simulation, it was found that shape of simulated pulse height response spectrum was strongly influenced by small variation in neutron energy. Hence, energy resolution of time-of-flight technique was included in simulation to compare simulated result with experimental response. Conversion of energy deposited in Scintillations material to light output was done by standard Cecil's prescriptions. To compare simulated response with experimental spectrum, light output resolution was also included in simulation. Correct values of parameters, for light output resolution, was estimated by comparing GEANT4 simulated pulse height spectrum of $^{137}Cs$ source with experimental pulse height spectrum. Experimentally measured pulse height spectrum for $^{137}Cs$ source has been also compared with that calculated by means of the standard Monte Carlo FORTRAN code PHRESP [69] to check the correctness of GEANT4 simulation.

Finally, experimental neutron response function were compared to GEANT4 simulated response function in energy range 2-20 MeV. It is very well known that neutron pulse height spectrum calculated with the NRESP7 code well describe the pulse height spectra of neutrons up to 20 MeV and therefore we also obtain response functions of mono-energetic neutron using this code to compare with GEANT4 result and experimental result. It was found that GEANT4 simulation explain the data fairly well except at lower end of the spectra, where the other reaction mechanisms are important. It was seen that a extra peak is coming at lower part of GEANT4 simulated spectra and the peak is gone when only proton are considered in simulation. This is because of the fact that GEANT4 still lacks some of important reactions and NeutronHP model of Inelastic do not work well. $^{12}C(n,\alpha)^{9}Be$ gives wrong $\alpha$ events at neutron energy above $\sim$8 MeV. On comparison with experimental response spectrum, it is also found that NRESP7 predictions are somewhat better in representing the overall shapes of the spectra, particularly at the lower

ends. The present results indicate that, though GEANT4 is fairly useful in predicting low energy response functions, the NeutronHP model should be upgraded to include higher order processes; moreover, the neutron induced reaction models should also be tested in more details to improve the performance of GEANT4. It is also observed that Geant4 simulation using Geisha [50] routine based data library produces results comparable to those from Geant4 with G4NDL3.14 for all energies. Attempts has been made to check the usefulness of other available models in comparison to NeutronHP models, which designed specifically for low energy neutrons upto 20 MeV. It was observed that NeutronHP models produce better agreement with the experimental data. The use of other cross-section data library, *i.e.*, G4HadronDataSet has also been found to make no qualitative difference.

In present thesis work, a beam experiment was performed using neutron detectors developed at Variable energy cyclotron center to study dependence of nuclear level density on angular momentum and temperature. $^{4}$He + $^{181}$Ta , $^{4}$He + $^{165}$Ho and $^{4}$He + $^{197}$Au systems were chosen to populate compound nuclei $^{185}$Re$^{*}$ with the excitation energy of $\sim$ 27 -37 MeV, $^{169}$Tm$^{*}$ with the excitation energy in the range of 26-38 MeV and $^{201}$Tl$^{*}$ with the excitation energy of $\sim$ 38 MeV. Six liquid scintillator typed neutron detectors and fifty $BaF_2$ typed $\gamma$-ray multiplicity detectors were used to measure energy spectra of emitted neutrons in coincidence with $\gamma$-ray fold. Angular momentum fold distribution was extracted from measured $\gamma$- ray fold distribution by using Monte Carlo based code GEANT3 [64, 73]. Theoretical neutron energy spectra for different angular momentum folds were calculated using statistical model based FORTRAN code CASCADE [74] by applying measured angular momentum distribution as input. In present analysis, it is seen that slope of the neutron energy spectrum was only sensitive to inverse level density parameter (k). Theoretical neutron energy spectra were fitted with experimental neutron energy spectra for different $\gamma$-ray folds using $\chi^2$ minimization technique. It is observed in analysis of $\gamma$-ray fold gated neutron spectra that inverse level density parameter remains constant as angular momentum $J$ increases in all systems at all excitation

energy used in present experiment. These results indicates that level density of compound nuclei populated in present work is independent of increment in angular momentum. It is also observed that there has been a relative decrement in nuclear level density at higher temperature for both $^{4}$He + $^{181}$Ta and $^{4}$He + $^{165}$Ho systems. The shell effect responsible for deformation must disappear with increasing temperature therefore nuclear level density decreases as temperature increases. However, further systematic study is required to understand the dependence of level density on angular momentum and temperature at mass region and excitation energy region used in present work.

# Bibliography


[1] Kenneth S. Krane, Introductory Nuclear Physics, WILEY - INDIA EDITION, John Wiley and Sons ( Reprint 2012 ), Inc, Chapter 11.

[2] R.G. Moore, Rev. Mod. Phys. 32, (1960), 101

[3] Qun Wang, Introduction to Modern Nuclear Physics, April 10, 2013, Department of Modern Physics, University of Science and Technology of China, Anhui 230026 China, qunwang@ustc.edu.cn, http://sta.ustc.edu.cn/ qunwang.

[4] Reiner Bass, Nuclear Reaction with Heavy Ions, Springer- Verlag, Berlin (1980),Chapter 7.

[5] P. E. Hodgson, Nuclear Heavy-ion Reactions, Clarendon Press Oxford (1978), Chapter 4.

[6] "An Experimental Verication of the Theory of Compound Nucleus, Phy. Rev. 80, 939(1950).

[7] S. N. Goshal, Phys. Rev. 80, 939(1950).

[8] W. Hauser and H. Feshbach Phys. Rev. C, 87, 366 (1952).

[9] J. M. Blatt and V. F. Weisskopf, Theoretical Nuclear Physics (Wiley, New York, 1952).

[10] T. D. Thomas, Nucl. Phys. 53, 577 (1964).

[11] W. Hauser and H. Feshbach, Phys. Rev. 87 (1952) 366

[12] J. R Grover and J. Gilat, Phys. Rev. 157 (1968) 802, 814 and 823

[13] F. H. Ruddy, B. D. Pate and E. W. Vogt, NucL Phys. A127 (1999) 323

[14] H. A. Bethe, Phys. Rev. 50, 332 (1936).

[15] R. Capote et. al. Nuclear Data Sheet 110, 3109 (2009).

[16] S. Cohen and W. J. Swiatecki Ann. Phys. (NY) 22, 406, (1963).

[17] A.V. Ignatyuk, G.N. Smirenkin and A.S. Tishin, Sov. J. Nucl. Phys. 21 255 (1975).

[18] A. V. Ignatyuk, K. K. Istekov and G. N. Smirenkin, Sov. J. Nucl. Phys. 29, 450 (1979).

[19] R. J. Charity, Phys. Rev. C 82, 014610 (2010).

[20] S. Bjornholm, A. Bhor and Mottelson, in Proceedings of the International Conference on the Physics and Chemistry of Fission, Rochester, New York, 1973 (IAEA, Vienna, 1974) Vol. 1, p. 367.

[21] A. R. Junghans, M. de Jong, H. G. Clerc, A. V. Ignatyuk, G. A. Kudyaev, K. H. Schmidt, Nucl. Phys. A 629, 635 (1998).

[22] S. Komarov, R. J. Charity, C. J. Chiara, W. Reviol, D. J. Sarantites, L. G. Sobotka, A. L. Caraley, M. P. Carpenter, D. Seweryniak, Phys. Rev. C 75, 064611 (2007).

[23] J. R. Huizenga and L. G. Moretto, Ann. Rev. Nucl. Sci., 22, 427(1972).

[24] http://www.nndc.bnl.gov/chart/chartNuc.jsp, Last observed on July. 5, (2007).

[25] J. M. Blatt and V. F. Weisskopf, Theoretical Nuclear Physics, p367, Wiley, (1960).

[26] R. Fischer, G. Traxler, M. Uhl, and H. Vonach, Phys. Rev., C30, 72(1984).

[27] T. von Egidy, H. H. Schmidt, and A. N. Behkami, Nucl. Phys. A481, 189(1988).

[28] A. Gilbert and A. G. W. Cameron, Can. J. Phys., 43, 1248(1965).

[29] C. H. Holbrow and H. H. Barschall, Nucl. Phys. 42, 264(1963).

[30] H.A. Bethe, Rev. Mod. Phys. 9 (1937) 69.

[31] A. Gilbert and A.G.W. Cameron, J. Phys. 43 (1965) 1446.

[32] W. Dilg, et al., Nucl. Phys. A217 (1973) 269.

[33] T.V. Egidy, A.N. Behkami, and H.H. Schmidt, Nucl. Phys. A454 (1986) 109.

[34] T. Ericson, Adv. Phys. 9 (1960) 425.

[35] A.N. Behkami et.al. Theor. Phys. (Beijing, China) 43 (2005) pp. 709718

[36] S. K. Kataria, V. S. Ramamurthy and S. S. Kapoor, Phys. Rev. C 18, 549 (1978).

[37] S. Shlomo and J. B. Natowitz Phys. Rev. C 44, 2878 (1991).

[38] S. Shlomo and J. B. Natowitz, Phys. Lett. B 252, 187 (1990).

[39] R. J. Charity and L. G. Sobotka Phys. Rev. C 71, 24310 (2005).

[40] Y. K. Gupta et. al., Phys. Rev. C 78, 054609 (2008).

[41] Y. K. Gupta et. al., Phys. Rev. C 80, 054611 (2009).

[42] K. Banerjee et. al. Phy. Rev. C 85, 064310 (2012).

[43] Pratap Roy et. al. Phy. Rev. C 86, 044622 (2012).

[44] R.A. Cecil, B.D. Anderson, R. Madey, Nucl. Instr. and Meth. 161, (1979) 439.

[45] G. Dietz and H. Klein, PTB-ND-22 Report (1982).

[46] J. K. Dickens, ORNL-6436, Oak Ridge National Laboratory, 1988

[47] A. Fasso, A. Ferrari, J. Rant, P. R. Sala, Fluka: a multi- particle transport Code, CERN-2005-10, INFN/T C 05/11, SLAC-R-773, 2005.

[48] A. Fasso, A. Ferrari, S. Roesler, P. R. Sala, G. Battistoni, F. Cerutti, E. Gadioli, M. V. Garzelli, F. Ballarini, A Ottolenghi, A. Empl, J. Rant, The physics model of FLUKA: status and recent developments, in: Computing in High Energy and Nuclear Physics 2003 Conference (CHEP2003), La Jolla, CA, USA, 24-28 March 2003 (paper MOMT005) eConf C0303241 (2003), arXiv:hep-ph/0306267.

[49] J. F. Briesmeister(Ed.), MCNP-A General Monte Carlo N- Particle Transport Code, Los Alamos, (LA-13709-M), 2000.

[50] S. Agostinelli et al., GEANT4- A simulation toolkit, et al., Nucl. Instr. and Meth. A 506, 250 (2003).

[51] http://www.nndc.bnl.gov.

[52] Glenn F. Knoll, Radiation Detection and Measurement, John Wiley and Sons, Inc - Third edition.

[53] H.Klein, F.Brooks, PoS (FNDA2006) 097.

[54] H. Klein, S. Neumann, Nucl. Instr. and Meth. A 476, 132 (2002).

[55] Horvath et al., Nucl. Instr. and Meth. A 440, 241 (2000).

[56] Robert E. Howe Nucl. Instr. and Meth. 190, 309 (1981).

[57] M. Ahmed Nucl. Instr. and Meth. 143, 255 (1977).

[58] R.A. Winyar et al., Nucl. Instr. and Meth. 95, 141 (1971). et al, Phys. Rev. C 67, 011603(R) (2003). New York, 1975), Vol. I.

[59] Dietze and Klein Nucl. Instr. and Meth. A 193, 549 (1982).

[60] P.A. Sderstrm. Proceedings of the International School of Physics Enrico Fermi, volume 169 page 551. SIF, Bologna and IOS Press, Amsterdam, 2008.

[61] A.J. Reiter, PhD Thesis, University of Glasgow, 2004.

[62] F. Begin et. al., Nucl. Inst. and Meth. A 562, 351 (2006).

[63] K. Banerjee, T.K. Ghosh, S. Kundu, T. K. Rana, C. Bhattacharya, J. K. Meena, G. Mukherjee, P. Mali, D. Gupta, S. Mukhopadhyay, D. Pandit, S. R. Banerjee, S. Bhattacharya, T. Bandopadhyay, S. Chatterjee et. al. Nucl. Instr. Meth. A 608, 440 (2009).

[64] Deepak Pandit, S. Mukhopadhyay, Srijit Bhattacharya, Surajit Pal, A. De, S. R. Banerjee, Nucl. Instr. Meth. A 624, 148 (2010).

[65] http://www.mesytec.de.

[66] P. Dhara et al., Proc: DAE-BRNS Symp on Nucl Phys, Dec 2003, Mumbai, Inida, 46B(2003)531.

[67] R. A. Cecil, B.D. Anderson and R. Madey Nucl. Instr. and Meth. 161, 439 (1979).

[68] E. Dekempeneer, H. Liskien, et al., Nuclear Instruments and Methods in Physics Research A 256, 489 (1987).

[69] T.Novotny,PhotonSpectrometryinMixedNeutronASPhotonFieldsUsing NE213 LiquidScintillatorDetectors,PTB-ReportPTB-N-28,Breunschweig, 1997.

[70] K. Banerjee, et al., Nucl. Instr. and Meth. A 608, (2009) 440.

[71] J. K. Dickens, ORNL-6436, Oak Ridge National Laboratory, 1988

[72] P.Moller, J. R. Nix, W. D. Myers and W. J. Swiatecki, Atomic Data and Nuclear.

[73] R. Brun, et al., GEANT3, CERN-DD/EE/84-1, 1986.

[74] F. Puhlhofer, Nucl. Phys. A 280, 267 (1976).

[75] S. Cohen, F. Plasil and W. J. Swiatechi, Ann. Phys. (NY)82, 557 (1974).